Unravel the tangle: atomistic insight into ultrahigh curcumin-loaded poly(2-oxazoline) and poly(2-oxazine)-based micelles

Josef Kehrein[1,2],* Ekinsu Gürsöz[1,2], Robert Luxenhofer[1], Alex Bunker[2]

[1] Soft Matter Chemistry, Department of Chemistry, Faculty of Science, University of Helsinki, 00014 Helsinki, Finland

[2] Division of Pharmaceutical Biosciences, Drug Research Program, Faculty of Pharmacy, University of Helsinki, 00014 Helsinki, Finland

*Corresponding author: Josef Kehrein, Soft Matter Chemistry, Department of Chemistry, Faculty of Science, University of Helsinki, 00014 Helsinki, Finland, E-Mail: josef.kehrein@helsinki.fi

Abstract

Amphiphilic ABA-triblock copolymers, comprised of poly(2-oxazoline) and poly(2-oxazine) blocks, can solubilize poorly water-soluble molecules; they form micelles with exceptionally high drug loading. In previous work, experimental studies have shown that even minor structural changes can have a significant impact on the maximum loading capacity for several different drugs. In an effort to shed light on the molecular interactions underlying the structure-property-relationships we performed all-atom molecular dynamics simulations on a selection of curcumin-loaded polymer micelles that have been experimentally characterized in detail. We investigated polymer-drug interactions in different micelle compositions, i.e. different drug loadings as well as variation of polymer structures of the inner hydrophobic core and the outer hydrophilic shell. Interestingly, the system with the highest experimental loading capacity also showed the highest amount of drug molecules encapsulated by the hydrophobic core *in silico*. Furthermore, in systems with a lower loading capacity the outer A blocks showed a greater extent of entanglement with the inner B blocks. Our results from hydrogen bond analyses corroborate the hypotheses of previous experimental studies: poly(2-butyl-2-oxazoline) B blocks, found experimentally to have a reduced loading capacity for curcumin in comparision to poly(2-propyl-2-oxazine), established fewer but longer-lasting hydrogen bonds. This possibly results from the additional methylene group in the backbone of poly(2-propyl-2-oxazine) to allow for different sidechain conformations around the hydrophobic cargo, compared to poly(2-butyl-2-oxazoline). This was further investigated by an unsupervised clustering of monomers within smaller model systems mimicking the different micelle compartments. In addition, an exchange of the hydrophilic poly(2-methyl-2-oxazoline) A blocks with the slightly more hydrophobic poly(2-ethyl-2-oxazoline) leads to a higher percentage of A blocks interacting with hydrophobic drugs and a reduced hydration of the corona; this suggests an impairment of micelle solubility or colloidal stability. This study demonstrates how all-atom molecular dynamics simulations can help in dissecting the effects of small structural changes in poly(2-oxazoline)-based micelles; we argue that it will pave the way for a more rational *a priori* design based approach to the development of drug delivery systems in the future.

Introduction

Poor solubility of therapeutically valuable drugs as well as new potential drug candidates represents an increasing challenge for the pharmaceutical industry. One way to tackle this problem is to make use of sophisticated drug delivery systems (DDS) that achieve efficient transportation of the (potentially toxic) compound to its biological target.[1,2] Besides widely established vehicles like liposomes, amphiphilic polymer micelles consisting of ABA-triblock copolymers of poly(2-oxazoline)s (pOx) and / or poly(2-oxazine)s (pOzi) resemble an interesting alternative and have been shown to provide maximum loading capacities (LC) of up to and more than 50 wt% for a variety of therapeutically valuable drugs, e.g. paclitaxel.[3] Such formulations are usually prepared via hydration of a thin film containing the polymers and drugs, after removal of the ethanol solution.[4,5] As for any other polymer micelle based formulation, the more hydrophobic B blocks are believed to function as the main drug reservoir, i.e. the part of the micelle where the drugs are encapsulated, whereas the more hydrophilic A blocks serve as a "protective", solubilizing corona of the micelle (Figure 1). Composed largely of hydrophobic elements but also more polar tertiary amides, these polymeric entities contain readily-modifiable sidechains and thus represent a versatile chemical toolbox that has garnered much attention in biomedical sciences in recent years.[6–9]
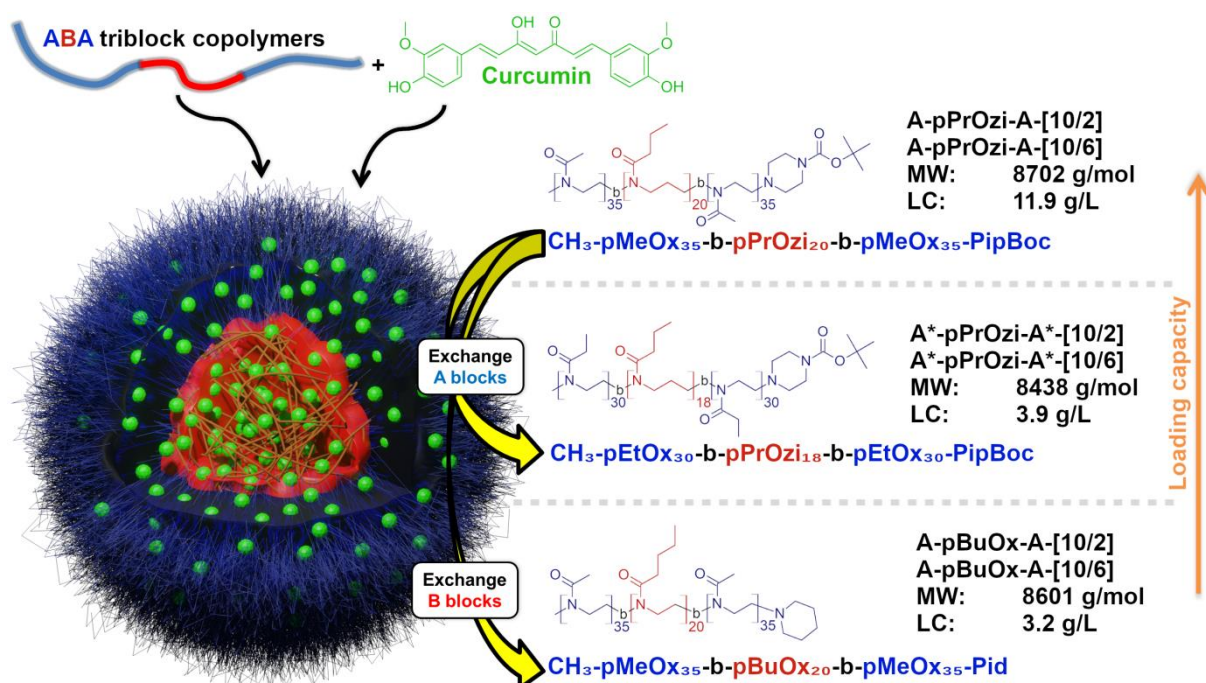
Figure 1: Structural model of ABA triblock copolymer-based poly(2-oxazoline) micelles and chemical structures of the three polymers investigated in this study (PipBoc = N-Boc-piperazine, Pid = piperidine). Terminology for the six systems (A = pMeOx, A* = pEtOx, [10/X] = w/w ratio), molecular weight and maximum LC values from literature[10,11] are listed on the right.

3

74 Micelle loading capacity has been investigated experimentally in great detail for a variety of drugs and

75 pOx/pOzi variants, and a strong dependence on the B block monomer type has been found.[3,12] For

76 example, poly(2-methyl-2-oxazoline)$_{35}$-b-poly(2-propyl-2-oxazine)$_{15}$-b-poly(2-methyl-2-oxazoline)$_{35}$-N-

77 Boc-piperazine (A-pPrOzi-A) has been shown to provide drastically superior drug loading for curcumin

78 (CUR), with a LC of 11.9 g/L given a polymer feed of 10 g/L, in comparison to poly(2-methyl-2-

79 oxazoline)$_{35}$-b-poly(2-propyl-2-oxazine)$_{15}$-b-poly(2-methyl-2-oxazoline)$_{35}$-piperidine (A-pBuOx-A)

80 comprising a constitutional isomer as B block repeat units (LC: 3.2 g/L).[10] The underlying reason for

81 this difference remained unknown until now. Based on small angle neutron scattering (SANS) and

82 nuclear magnetic resonance spectroscopy (NMR) experiments, detailed structural models of these

83 micelles have recently been postulated: within systems with lower LC, the A blocks start to interact

84 with the drugs even at lower loadings, potentially leading to the desolvation of the protective corona

85 which may then in turn lead to micelle agglomeration.[13,14] While initial studies focused on

86 systematically exchanging B blocks in order to characterize loading capacities for different drugs,

87 recent studies have shifted the focus towards modifying the hydrophilic A blocks, potentially also

88 interacting with the cargo. Exchanging pMeOx with the slightly more hydrophobic poly(2-ethyl-2-

89 oxazoline) (pEtOx) has been shown to tremendously reduce the maximum LC of CUR for pPrOzi-

90 based systems (A*-pPrOzi-A*, LC: 3.9 g/L). It is believed that the more hydrophobic A block promotes

91 more interactions with the hydrophobic guest molecule, potentially more readily impairing micelle

92 solubility.[11]

93 While all these previous experimental studies provide a clear structural model on the general

94 constitution of these micelles, detailed investigations into the driving polymer-drug interactions remain

95 rather elusive to such techniques, but these are needed to explain in more detail the observed

96 differences in micelle properties. Thus, in this work, we aim to provide, for the very first time, a detailed

97 look into the dynamics of these polymer micelles, using all-atom molecular dynamics simulations

98 based on the structural models established by previous SANS and NMR experiments. The only other

99 recent study that has performed simulations on similar systems only reported basic density profiles.[15]

100 Herein, we want to provide a better mechanistic understanding of the reported phenomena, derived

101 from the observed polymer-drug interactions, in order to drive forward a more rational *a priori*

102 formulation design of these DDS in the future. For this purpose, we simulated three different polymer

103 micelles at two different drug loadings each ([10/2] and [10/6] polymer/drug mass [w/w] ratios). CUR, a

104 pharmacologically relevant molecule naturally occurring in rhizomes of *Curcuma longa* L. and showing

105 antioxidant and anti-tumor effects,[16] was chosen as the model compound and has been extensively

106 characterized experimentally as a cargo in previous work.[10,11,13,14,17,18] The investigated systems are A-

107 pPrOzi-A (additionally labeled [10/2] or [10/6], depending on the polymer/drug mass [w/w] ratio), A*-

108 pPrOzi-A* exchanging pMeOx-based A blocks with pEtOx while keeping a similar mass ratio between

109 hydrophilic and hydrophobic repeat units (with the hydrophobic units making up around 30 % of the

110 polymer mass), as well as A-pBuOx-A containing the structural isomer pBuOx as B block.[10,11] Thus,

111 these systems represent exemplary cases in which an exchange of the A or the B blocks leads to a

112 significant decrease in the maximum loading capacity.

Computational models and methods

Parameterization

Similar to a previous simulation study involving polymer micelles, parameterization was performed on the basis of a modular building block approach.[19] Small trimers with the desired repeat units were first built in Avogadro 1.2.0.[20] For each oligomer, four energy minimized conformations were generated via openBabel 3.0.0[21] using the GAFF force field[22] and subsequently uploaded to the PyRED server[23–25] in order to perform a multi-conformational RESP fitting,[26] using Gaussian16 C.01[27] with the Hartree-Fock/6-31-G* level of theory for charge derivation. Hereby, each monomer defined a single residue and was constrained to have a net charge of zero. Using this approach, atom types and bonded parameters were adapted from the Amberff14SB force field set,[28] similar to a previous modeling study involving pEtOx.[29] The termini N-Boc-piperazine (PipBoc) and piperidine (Pid) were modeled in their protonated states and capped with corresponding MeOx/EtOx monomers. The loaded drug CUR was modeled in the keto-enol tautomer form, as previous studies suggested this to be the major form present within these micelles.[3,30,31] Charges were derived analogously via PyRED using Gaussian16 C.01 (HF/6-31-G*), and atom types and bonded parameters were subsequently adapted from the GAFF2 force field[22] using antechamber via acpype 2022.6.6.[32,33]

Micelle modeling

The schematic workflow of the modeled systems is shown in Figure 2. To model the starting structures of the micelles based on the structural insights given from previous experimental work, polymers of the desired lengths were first built in a stretched-out conformation using tleap from AmberTools22.[34] Each polymer chain was then initially relaxed by performing an energy minimization (maximum of 2000 cycles) followed by a short 600 ps-long simulation in Generalized Born implicit solvent[35] (12 Å distance cutoff) using sander from AmberTools22.[34] For each micelle, 35 polymers were then inserted in a loosely spherical orientation using packmol 18.169[36,37] (similar to other recent micelle modeling studies[38,39]), leaving approximately 33 % of the core volume empty for solvation, assuming a placement of ~50 % of the CUR molecules in this area (the exact number of polymers constituting each micelle was not known *a priori* from experiments). After placement of the polymers with hydrophilic A blocks oriented towards the outside and hydrophobic B blocks towards the inside, the desired amount of CUR molecules for a [10/2] or [10/6] polymer/drug w/w ratio was inserted randomly within a sphere that spanned the volume of the hydrophobic core as well as parts of the hydrophilic corona. Details of the chosen packmol settings for this pre-assembly of polymers and drugs can be

144 found in the Supporting Information (Figure S1). For each micelle, the best solution found by packmol

145 after 50 optimization loops was then solvated in a cubic box with TIP3P water,[40] with a minimum

146 polymer-to-border distance of 10 Å. Chloride ions were used for subsequent neutralization. Structures

147 and topologies were then converted to GROMACS files using ParmEd from AmberTools22.[41]

148 For additional sampling data on polymer-drug interactions while limiting the computational costs, we

149 artificially separated the environment of the hydrophilic corona and the hydrophobic core. To do so,

150 small cubic simulation boxes (~ 5 nm box length) filled with randomly placed shorter hexamer variants

151 of pMeOx / pEtOx / pPrOzi / pBuOx (capped with methyl groups), in addition to CUR and water

152 molecules were created via packmol, in accordance with the respective polymer, drug and water atom

153 densities found after 1.75 µs within the area of the corona and the micelle core of the first replicas

154 (treating polymer densities as one type, either A or B blocks). Hence, for these model systems atom

155 numbers were scaled down to a volume of 125 nm³ from the simulations of the entire micelles. Core

156 densities were taken as an average across the volume up to 2 nm from the micelle center, whereas

157 shell densities were taken from the distribution between 4 and 5 nm from the respective center.
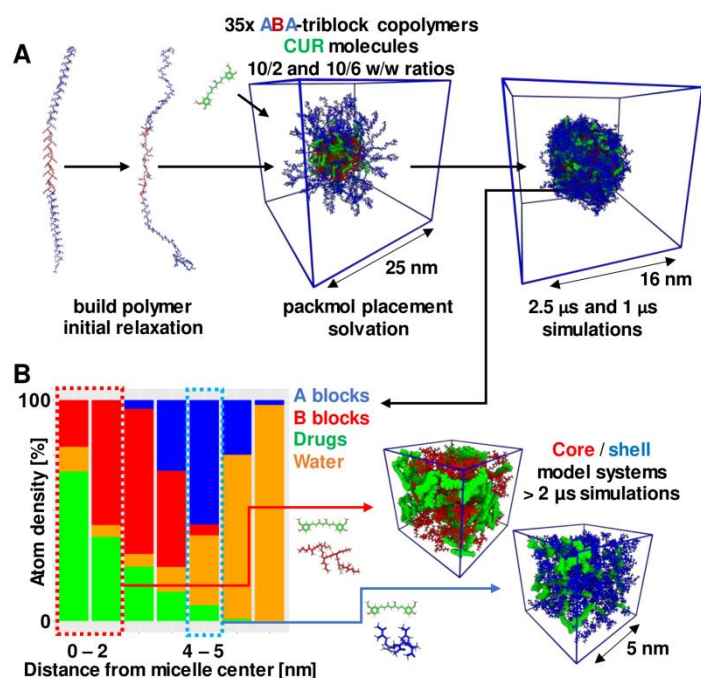
158

159 **Figure 2**: Modeling workflow for the simulated systems. (A) Polymers were initially built and relaxed
160 via tleap and loosely spherical micelles modeled using packmol with an amount of CUR molecules
161 equaling a [10/2] or [10/6] polymer/drug w/w ratio, given a system of 35 polymers. Two replicas of
162 each system were simulated, totaling 3.5 µs respectively. (B) In addition, smaller model systems with
163 hexamers were built according to polymer, drug and water atom densities in core and shell areas of
164 the first replicas after 1.75 µs; the simulations were then carried on for at least 2 µs.

165 *Simulation setup*

166   All simulations were performed using GROMACS 2022.01.[42] A general equilibration protocol for each

167   micelle can be described as follows: after initial energy minimization (5000 steps, steepest descent)

168   100 ps in a NVT ensemble were conducted at 300 K, applying the Velocity-rescale thermostat[43] with

169   separate coupling constants of 0.1 ps^{-1} for the polymers, as well as for drugs and solvent. The leap-

170   frog integrator[44] was used with 2 fs time steps. Particle-Mesh Ewald summation[45] was applied for

171   electrostatics (1.0 nm cutoff distance, 0.125 nm Fourier spacing). H-bonds were constrained using the

172   LINCS algorithm.[46] 100 ps in NPT ensemble were followed by applying the Parrinello-Rahman

173   barostat[47–49] with a coupling constant of $4.5e^{-5}$ bar^{-1} and a reference pressure of 1.0 bar.

174   This NPT run was then continued for 10 ns, following a simulated annealing protocol[50,51] to help

175   overcome larger energetic barriers: the system was quickly heated up to 385 K within the first 800 ps

176   and cooled down again to 300 K in the last 500 ps. Snapshots were written out every 10 ps. The

177   hydrophilic A blocks, initialized in an extended conformation, rapidly condensed onto the hydrophobic

178   core; this lead to a shrinkage of the micelle that allowed for a smaller simulation box to be used. The

179   final snapshot was then stripped off from an excess of bulk water, by removing every water molecule

180   whose oxygen atom was positioned more than 1.0 nm away from any polymer. Single CUR molecules

181   and chloride ions in bulk water were removed as well. The structure was then resolvated in a cubic

182   box and used for continuation of the simulation. This 10 ns-long equilibration protocol was repeated

183   several times (up to a total of 60 ns) in order to successively reduce the initial box lengths of around

184   22 - 28 nm down to 16 - 18 nm. The simulation was then continued at 300 K up until 500 ns were

185   simulated. In order to promote further equilibration, systems were heated up again to 385 K and

186   simulated for an additional 1.5 µs at elevated temperature. The systems were then cooled down again

187   to 300 K and simulated until a total of 2.5 µs were reached (Table 1).

188   In order to account for a possible dependence of results on the randomly created initial polymer

189   starting conformations and positions of CUR molecules, we subsequently performed an additional

190   replica of each system using another set of starting structures generated via packmol. Averaging the

191   fraction of CUR molecules starting within the core in both replicas for each polymer type and drug

192   loading respectively, similar amounts of drugs for A-pPrOzi-A, A*-pPrOzi-A* and A-pBuOx-A systems

193   are located near the B blocks at the beginning of the simulations (~55% for every [10/2] loading and

194   ~45% for every [10/6] loading). For these second replicas, the first equilibration phase up until 500 ns

195   was performed analogously as described above. Then, for the following equilibration phase, systems

196   were heated up to 385 K, simulated for 500 ns and cooled down to 300 K for a final 200 ns. Shorter

197 time lengths were chosen based on the convergence of properties in the first replicas (see also Figure

198 S2 and 5).

199 The last 100 ns at 300 K from each simulation were treated as final production run and used for further

200 analyses. Simulations of smaller model systems were conducted with analogous initial energy

201 minimizations and 100 ps runs in NVT and NPT ensembles. The NPT run was then continued for at

202 least 2 µs at 300 K (Table 2).

203 **Table 1**: List of simulated systems. Different replicas are labeled with suffixes 1 and 2. Time lengths of
204 equilibration phases, numbers of CUR molecules, in addition to final box lengths are listed. A removal
205 of CUR molecules located in the bulk phase during initial equilibration is noted with minus signs.

System name (35 polymers each)	CUR molecules (% in core at start)	First equilibration at 385 K [ns]	Continuation at 300 K [ns]	Second equilibration at 385 K [ns]	Final run at 300 K [ns]	Box length [nm]
A-pPrOzi-A-[10/2].1	166 (67.8)	60	440	1500	500	16
A-pPrOzi-A-[10/6].1	496 (40.7)	60	440	1500	500	16
A*-pPrOzi-A*-[10/2].1	160 (38.1)	60	440	1500	500	16
A*-pPrOzi-A*-[10/6].1	482 (42.2)	60	440	1500	500	16
A-pBuOx-A-[10/2].1	164 (57.6)	40	460	1500	500	16
A-pBuOx-A-[10/6].1	490 - 3 (39.9)	20	480	1500	500	17
A-pPrOzi-A-[10/2].2	166 (45.0)	40	460	300	200	16
A-pPrOzi-A-[10/6].2	496 - 2 (51.0)	60	440	300	200	18
A*-pPrOzi-A*-[10/2].2	160 (67.5)	20	480	300	200	17
A*-pPrOzi-A*-[10/6].2	482 (47.8)	20	480	300	200	17
A-pBuOx-A-[10/2].2	164 (53.3)	20	480	300	200	17
A-pBuOx-A-[10/6].2	490 (51.0)	20	480	300	200	18

206

207 **Table 2**: Additional simulation boxes, with polymer, drug and water atom densities in accordance with
208 the conditions found within the core (C) and the shell (S) of the first replicas after 1.75 µs.

System name	Hexamers	CUR molecules	Water molecules	Simulation time [µs]
A-pPrOzi-A-[10/2].C	34	139	157	3.06
A-pPrOzi-A-[10/2].S	105	17	1052	2.34
A-pPrOzi-A-[10/6].C	50	104	182	2.48
A-pPrOzi-A-[10/6].S	92	79	409	2.40
A*-pPrOzi-A*-[10/2].C	65	66	267	2.38
A*-pPrOzi-A*-[10/2].S	87	26	805	2.35
A*-pPrOzi-A*-[10/6].C	31	150	170	2.54
A*-pPrOzi-A*-[10/6].S	73	82	345	2.38
A-pBuOx-A-[10/2].C	58	80	248	2.35
A-pBuOx-A-[10/2].S	103	21	1063	2.33
A-pBuOx-A-[10/6].C	71	47	375	2.25
A-pBuOx-A-[10/6].S	82	87	532	2.36

209 *Analysis*

210 All analyses were performed using cpptraj from AmberTools22[34] and mdanalysis 2.0.[52,53] If not

211 otherwise mentioned, combined values for every nanosecond in the last 100 ns from both replicas of

212 each system were used for comparison. From these data, boxplots were created showing the

213 interquartile range of values, with median values marked as black lines. Levels of significance for

214 differences between median values were further evaluated by conducting unpaired two-samples

215 wilcoxon tests (p-values: *** = <0.001, ** = <0.01, * = <0.05, NS. = not significant).[54,55] Images were

216 created using VMD 1.9.3[56] and PyMOL 2.3.0.[57] 2D polymer-drug interaction plots were generated

217 using ProLIF 1.0.0.56.[58] The asphericity Q of micelles was calculated via rdkit 2022.03.5[59] based on

218 the last 100 ns with 10 ns steps (10 snapshots) and is defined as:

$$219 \qquad Q = \frac{(\lambda_2 - \lambda_1)^2 + (\lambda_3 - \lambda_1)^2 + (\lambda_3 - \lambda_2)^2}{2 (\lambda_1 + \lambda_2 + \lambda_3)^2}$$

220 with λ_1, λ_2 and λ_3 representing the three eigenvalues of the radius of gyration tensor.[60,61] Hydrogen

221 bonds were calculated using distance and angle cutoffs of 3.5 Å and 120°. Hydrogen bond

222 autocorrelation functions $C(\tau)$ were calculated, defined as:

$$223 \qquad C(\tau) = \langle \frac{h_{ij}(t_0) \, h_{ij}(t_0 + \tau)}{h_{ij}(t_0)^2} \rangle$$

224 where $h_{ij}(t_0) = 1$ and $h_{ij}(t_0 + \tau) = 1$ if a hydrogen bond is detected at times t_0 and $t_0 + \tau$ between

225 atoms i and j, with τ representing the maximum lag time of 250 ps (step size: 10 ps).[62] These were

226 computed for the last 100 ns of the larger micelles, as well as for the whole trajectories regarding the

227 smaller model systems.

228 For generating distance histograms, all monomers within 20 Å distance to each CUR molecule at the

229 end of the simulations were selected and their distance towards different drug moieties calculated for

230 the last 100 ns. In order to perform additional density analyses of different polymer moieties around

231 drug molecules, first each CUR molecule was aligned to the same position, with respect to one of its

232 phenols or its keto-enol functional group. This was performed on a 3 x 3 x 3 nm³ grid with 1 Å

233 resolution. After this procedure, obtained occupancy values at each grid point around every CUR

234 molecule in the system were added up and divided by the number of analyzed frames (last 250 ns)

235 and drug molecules; as a result, the average number of polymer atoms of interest found at each grid

236 element per frame around a single CUR moiety was obtained. For the visualization of hotspots,

237 threshold values representing 65 % (core) or 50 % (shell) of the respective highest occupancy grid

238 value of the density map were chosen.

239 For the case of the smaller model systems, an additional g3 analysis was performed on the last 50 ns

240 of each simulation (with 10 ps time steps). The procedure was developed by Sukhomlinov et al.[63,64]

241 and is described in more detail in a recent study by Davies et al.[65] A radial-angular three-particle

242 distribution function is used to create heatmaps from intra-residue angles and distances. For every

243 time step and every selected atom B of each monomer, the distance $\vec{r}_{BC}$ to any other atom C within the

244 selection is computed, given an angle θ_{ABC} between atoms A (the nearest atom to C), B and C (see

245 also Figure 12A, top right). For this analysis, four atoms present within every monomer type were

246 selected: the amide nitrogen and oxygen, in addition to the first sidechain carbon atom and the second

247 backbone carbon atom of the respective residue. Termini of the hexamers were excluded and a

248 distance cutoff of 6 Å was chosen. Generated heatmaps of all 12 different model systems were then

249 combined into a single similarity matrix using mean structural similarity index metrics (SSIM).[66] The

250 latter are computed by dividing each heatmap into N smaller equally-sized windows with lengths x_i

251 and y_i and comparing their variance σ^2 and covariance σ_{xy}, with correction factors c_1 and c_2:[65]

252
$$SSIM = \frac{1}{N}\sum_{i=1}^{N} SSIM\,(x,y) = \frac{1}{N}\sum_{i=1}^{N} \frac{(2\mu_{x_i}\mu_{y_i} + c_1)(2\sigma_{x_iy_i} + c_2)}{(\mu_{x_i}^2 + \mu_{y_i}^2 + c_1)(\sigma_{x_i}^2 + \sigma_{y_i}^2 + c_2)}$$

253 Analogously to Davies et al.,[65] the generated similarity matrix was then reduced to a 2D dataset via t-

254 distributed stochastic neighbor embedding (t-SNE)[67] and subsequent density-based spatial clustering

255 (DBScan).[68] A perplexity of 50 was used for t-SNE and a minimum sample size of 25 monomers with a

256 distance threshold ε of 0.25 was chosen. Finally, a principal component analysis (PCA) was performed

257 to assess conformations of the different clusters.[69] Thus, using the described g3 analysis method,

258 monomers of all systems were effectively clustered according to differences in intra-residue angle and

259 distance distributions.

Results and discussion

In order to dissect the structure-property-relationships of ultrahigh drug-loaded pOx/pOzi-based micelles on a molecular level we performed all-atom molecular dynamics simulations of three exemplary systems at polymer/drug mass ratios of [10/2] and [10/6]: A-pPrOzi-A-[10/2] and A-pPrOzi-A-[10/6], A*-pPrOzi-A*-[10/2] and A*-pPrOzi-A*-[10/6] (exchanging A = pMeOx with A* = pEtOx), as well as A-pBuOx-A-[10/2] and A-pBuOx-A-[10/6] (exchanging pPrOzi with pBuOx). Two replicas for each system were conducted (2.5 µs and 1 µs respectively), using elevated temperatures (385 K) during equilibration to overcome potential energy barriers. We subsequently analyzed various properties regarding overall micelle compositions and specific polymer-drug interactions.

Micelle structures and hydration

Within each system, the initially stretched-out hydrophilic A blocks rapidly condense onto the hydrophobic B blocks, albeit the protonated and rather flexible PipBoc/Pid termini orient themselves outwards and remain relatively solvent-exposed. CUR molecules get entangled quickly between the polymer chains and show very limited movement once this has occurred. All micelles reach a radius of gyration (R_g) between 4.2 and 4.8 nm, with [10/6] systems showing slightly higher values (Figure 3A). As expected, at higher drug loadings more CUR molecules can be observed in the outer (A block) region of the micelles at the end of the simulations (Figure S3). Possibly, these could result in hydrophobic patches on the micelle surface, suppressing hydrophilic A blocks from functioning as solubilizing corona and ultimately leading to aggregation at drug concentrations that exceed the maximum LC.

In the case of A-pPrOzi-A the hydrophobic core and hydrophilic corona seem to exhibit a more pronounced phase separation, compared to A*-pPrOzi-A* and especially A-pBuOx-A in which B blocks show a greater extent of entanglement with the A blocks, i.e., A blocks interpenetrate the hydrophobic domain to a higher degree; this could be detrimental to the functionality of the former as a solubilizing corona. This interpenetration becomes evident when observing not only the atom densities of A blocks (Figure S4), but also e.g. the R_g ratios between B blocks and entire micelles: we clearly see the lowest value for A-pPrOzi-A (Figure 3B). Also, the B block solvent-accessible surface area (SASA) in contact with A blocks is significantly lower for A-pPrOzi-A in comparison to A*-pPrOzi-A* and A-pBuOx-A at the same level of drug loading (Figure 3C). It should be noted that pPrOzi is less hydrophobic than pBuOx; the stronger phase separation between pMeOx and pPrOzi is therefore not self-evident but may be explained by reduced miscibility of Ox and Ozi repeat units. The asphericity Q

291   of all systems is close to zero, within a similar range as found in previous modeling studies for

292   spherical micelles (Table S1).[60,70,71]
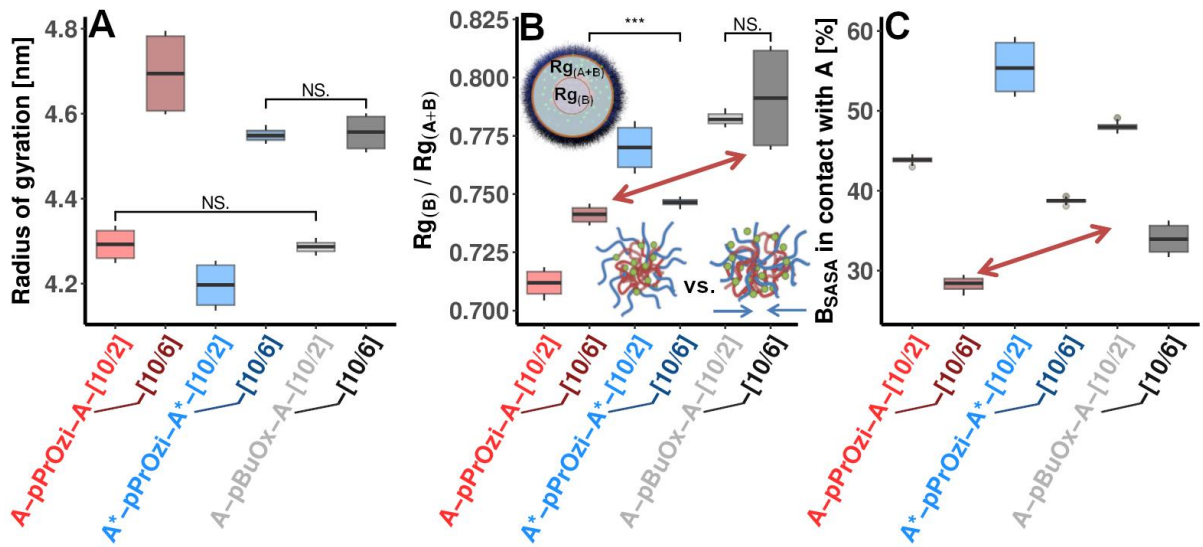
293

294   **Figure 3**: Boxplots showing (A) the radii of gyration of polymer atoms, (B) the ratio of radii of gyration
295   between B block atoms and every polymer atom and (C) the percentage of B block SASA that is in
296   contact with A blocks. Levels of significance for differences in median values are marked (p-values: ***
297   = <0.001, ** = <0.01, * = <0.05, NS. = not significant).

298   Overall, atom densities of individual micelle constituents demonstrate that, in contrast to e.g. lipid

299   bilayers of liposomes, each structure contains small amounts of water even within the inner

300   hydrophobic core (making up to around ~10 % of atoms, Figure S4) and much more so in the outer

301   regions of the hydrophilic shell. These structures are thus not completely desolvated, which conforms

302   to previous hypotheses and results from pyrene fluorescence assays;[5] this suggests water plays an

303   important role in the formation of this form of DDS.[13,14] Upon closer examination of the H-bonds (HB)

304   that A block oxygens are able to form with water, a lower level for the less hydrophilic A*-pPrOzi-A* is

305   found (Figure 4A), which is in agreement with the hypothesis of a reduced solvation of this corona. A-

306   pPrOzi-A with the highest maximum LC also shows the largest number of H-bonds both for [10/2] and

307   [10/6] loadings. Performing an analogous analysis on the B blocks reveals, as expected, lower

308   numbers (Figure 4B). Interestingly, for A-pBuOx-A the amount of H-bonds is much larger in

309   comparison to A-pPrOzi-A and A*-pPrOzi-A*. However, this seems not to be a result from higher water

310   contents within the core (compare Figure S4), but rather from the above described lack of clear

311   separation between the core and shell areas. Hence, in these instances, solvent-exposed B blocks in

312   the outer regions of the micelles are present to a greater extent (image in Figure 4D). Radial

313   distribution functions (RDF) for water oxygens around polymer amide oxygens reveal similar results to

314 these H-bond analyses (Figure 4C and 4D): for A blocks the highest hydration is found for the case of

315 A-pPrOzi-A and the lowest for A*-pPrOzi-A*.
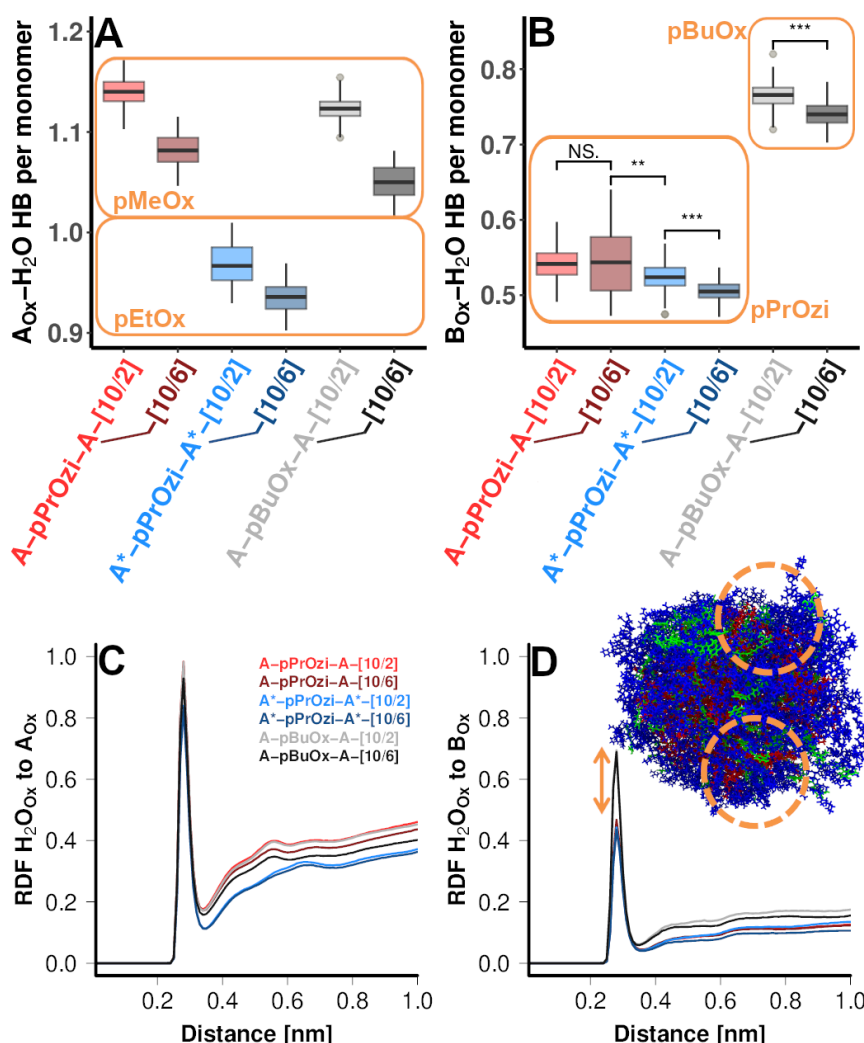
Figure 4: H-bonds between water hydrogens and (A) A block oxygens as well as (B) B block oxygens. Additionally, RDF plots for water oxygens found around (C) A block oxygens and (D) B block oxygens are illustrated. In (D) an exemplary snapshot of A-pBuOx-A-[10/2] illustrates how B blocks are solvent-exposed on the surface, leading to much higher solvation. Levels of significance for differences in median values are marked (p-values: *** = <0.001, ** = <0.01, * = <0.05, NS. = not significant).

322 Generally speaking, water soluble pOx and pOzi are known to be thermoresponsive, they show a

323 lower critical solution temperature (LCST) type behavior, promoting phase separation upon higher

324 temperatures.[72] In particular, pPrOzi has a LCST at around 11°C.[73] During equilibration, the systems

325 were heated up to 385 K for extended time periods in which micellar structures remained intact.

326 However, according to the reported LCST behavior, hydration decreased as can be observed by the

327 amount of H-bonds formed between water molecules and polymer repeat units over time (Figure 5).

328 This phenomenon has been observed in other simulation studies with LCST type polymers as well,

329 describing a reduction in "hydrophobic hydration".[74] Upon cooling down to 300 K towards the end of

15

330 the simulations, solvation quickly increases, more readily for the A blocks than the B blocks, but not

331 quite to the same level as before the temperature increase (compare Figure 5A/B and C/D).

332 Interestingly, the number of H-bonded and water-bridged A-A pairs are mostly identical to their values

333 before the second equilibration at 385 K (Figure 5B). These bridging interactions could possibly

334 resemble energetically favorable hydration patterns that are thus established very quickly again after

335 cooling down. Such bridges represent a considerable quantity of A-water H-bonds and are most

336 commonly found for A-pPrOzi-A (Figure 5E), which also shows the highest corona hydration overall

337 (Figure 4A).

338
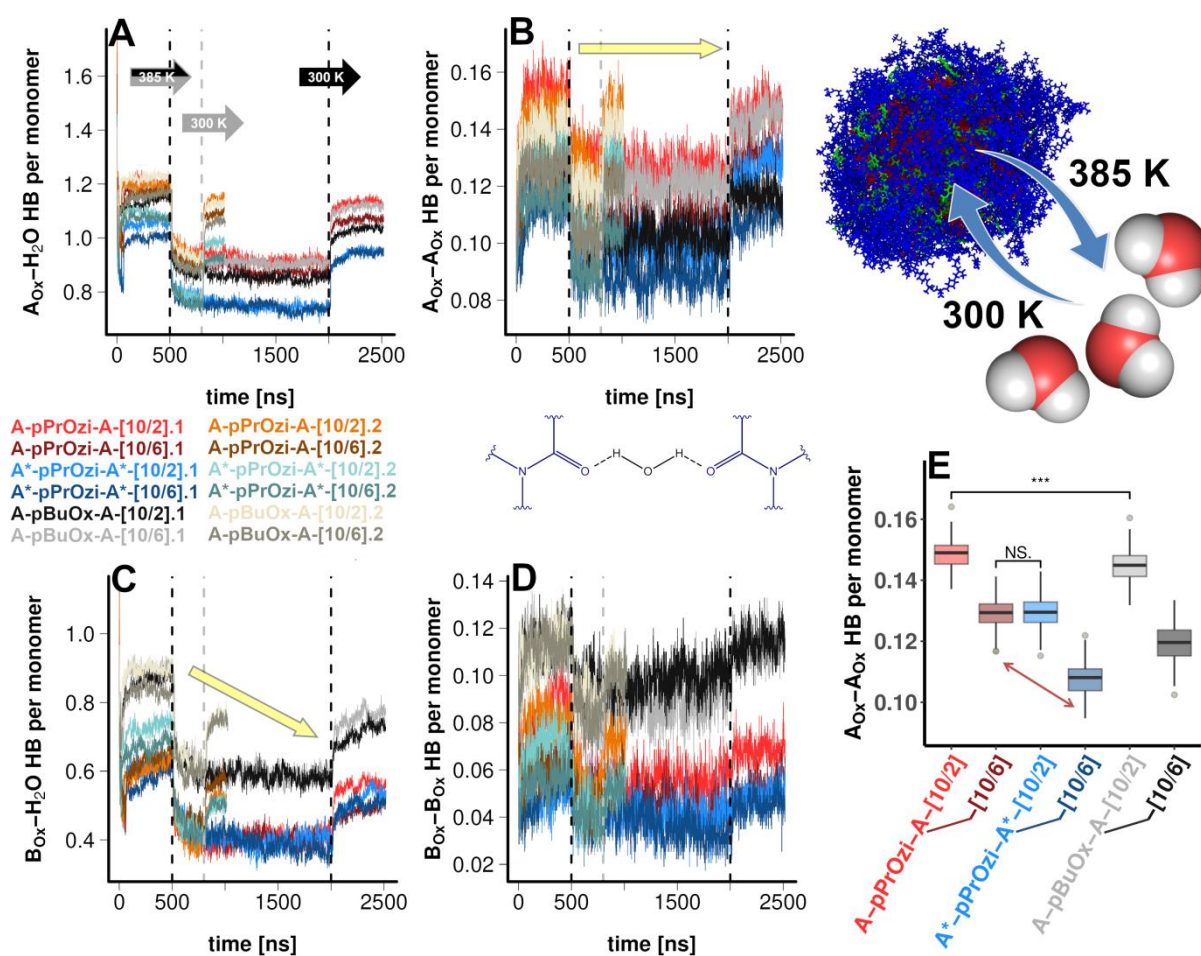
Figure 5: (A) Quantity of H-bonds between A block oxygens and water hydrogens shown over time
(color legend given for all plots in the middle left). Dashed black lines and arrows within the plot
indicate times for the first replicas at which systems were heated up to 385 K (500 ns) and decreased
again to 300 K (2 µs) for the second equilibration phase at elevated temperatures and the subsequent
final production run (see also Table 1). Grey dashed lines and arrows indicate the same for the
second replicas (500 ns and 800 ns). (B) Bridging H-bonds between A blocks. (C) and (D) show
analogous calculations for B blocks. (E) Total amount of bridging H-bonds detected for the shells.
Levels of significance for differences in median values are marked (p-values: *** = <0.001, ** = <0.01,
* = <0.05, NS. = not significant).

348 As conducting equilibrations of larger systems with high degrees of freedom at elevated temperatures

349 is a well-established method[50,75,76] to escape possible metastable states (first simulations on such

16

350   micelles applied a temperature of 333 K[15]), the reduction in solvent within the core after exposure to

351   elevated temperatures could indicate that the initial placement by packmol, leaving approximately

352   33 % space within the core available for solvent molecules, partly lead to an artificially high solvation

353   in the beginning of the simulations; this effect was especially pronounced for the case of A*-pPrOzi-A*-

354   [10/2].1 and A*-pPrOzi-A*-[10/6].1, wherein larger water clusters were observed temporarily during the

355   first equilibration phase at 300 K within the core, but vanished after extended simulation times at 385

356   K and the final subsequent period at 300 K (Figure S5). While we cannot rule out the possibility of

357   such phenomena occurring (potentially also contributing to an impairment of loading capacity of

358   hydrophobic drugs), we would like to note that the micelle water content within the core after additional

359   equilibration (~ 10 %) is within a similar range to what was reported recently for all-atom simulations of

360   unloaded, triblock copolymer-based Pluronic L64 micelles (10 – 18 %, also pre-assembled via

361   packmol).[39]

362   To investigate overall CUR mobility in the micelles, we analyzed the differences in distances of CUR

363   molecules from the center of the micelle between the start and the end of the simulations. Values of

364   up to 6 nm are recorded in single instances (Figure S6A), suggesting that the conducted protocol is

365   able to capture possible movements of drug molecules across the amphiphilic structure, though a

366   large fraction of the cargo remained rather rigid after initial compaction of the micelle and

367   entanglement between the polymer chains (mostly values below 1 nm are recorded). Inspecting the

368   standard deviations of each of these distances indicates that drug molecules within the outer parts of

369   the micelle show the largest movement along the radial axis (Figure S6B). In accordance with the

370   highest experimental LC, A-pPrOzi-A systems show a larger quantity of CUR molecules within the

371   core (Figure 6A and 6B), which, despite slightly larger R_g values of micelles (Figure 3A), show reduced

372   distances to the micelle center (Figure 6C). In accordance with drug loadings within the core, standard

373   deviations for molecule distances are also, marginally but significantly, smaller (Figure 6D).

374
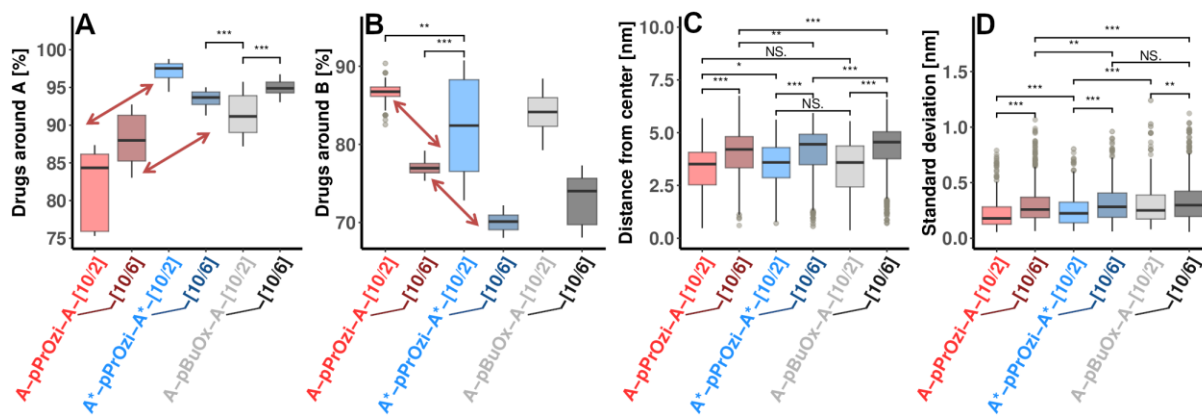
Figure 6: (A) Amount of drugs within 5 Å of A block atoms. (B) Amount of drugs within 5 Å of B block atoms. (C) Average distances of drugs from the micelle center (geometric center of B block atoms). (D) Standard deviation for distances of drugs to center. Levels of significance for differences in median values are marked (p-values: *** = <0.001, ** = <0.01, * = <0.05, NS. = not significant).

379 *Polymer-drug interactions*

380 Now that we have characterized the overall micelle compositions, we proceed to dissect polymer-drug

381 interactions and dynamics in greater detail. First, we describe the general interaction patterns that

382 were found across all systems after systematic investigations of the local drug environments.

383 Afterwards, further analyses of CUR-polymer H-bonds are presented. Finally, distances between

384 specific polymer and CUR moieties are compared.

385 *Overview*

386 Within each system, CUR molecules can be seen establishing H-bonds to polymer carbonyl oxygens

387 of the tertiary amides via their phenolic hydroxyl groups (Figure 7A, 7B, 7C-II and 7D-III), sometimes

388 including bridging water molecules (Figure 7C-III and 7D-II). This conforms to previous NMR studies[13]

389 of A-pPrOzi-A systems and might result in an effective (yet transient) polymer cross-linking. In every

390 system, about 90 % of such links established via directly double-H-bonded CUR molecules are formed

391 intermolecularly between different chains. This could possibly impact solubility and colloidal stability

392 when occurring in the corona, in particular between two individual micelles (not implemented in the

393 present model). In accordance with this experimental study, the keto-enol moiety rarely establishes

394 similar interactions. CUR-polymer H-bonding affecting overall hydrophilicity of delivery systems has

395 also been discussed as an important factor for drug solubilization in recent modeling studies regarding

396 (PEG-)chitosan-based DDS.[77,78] Apart from these interactions, the lipophilic drug molecules are

397 embedded within the mostly hydrophobic backbones and sidechains of the polymers. Within areas of

398 high CUR concentrations, π-π stacking and CUR-CUR H-bonds (Figure 7A-II) can be observed, with

399 the carbonyl group of the keto-enol moiety also partly functioning as an acceptor. At high drug

400 loadings, CUR molecules in the outer regions of the micelles do not diffuse into the bulk water but

401 rather move around on, or stick to, the surface of the corona; as a result the latter becomes more

402 hydrophobic. *In vitro*, such a situation would be expected to lead to micelle-micelle interactions,

403 compromising colloidal stability. As noted before, when maximum LC is exceeded *in vitro* for the

404 systems investigated here, it is not the drug that is precipitating, but the drug-loaded micelles form a

405 gel phase of polymer and drug, in line with the hypothesis of physically cross-linked micelles.[30] it could

406 be postulated that, in an *in vivo* environment, such sticky patches possibly increase the strength of the

407 interaction with either a cell membrane or a protein, e.g. serum albumin, affecting drug release,

408 endocytosis and pharmacokinetics.
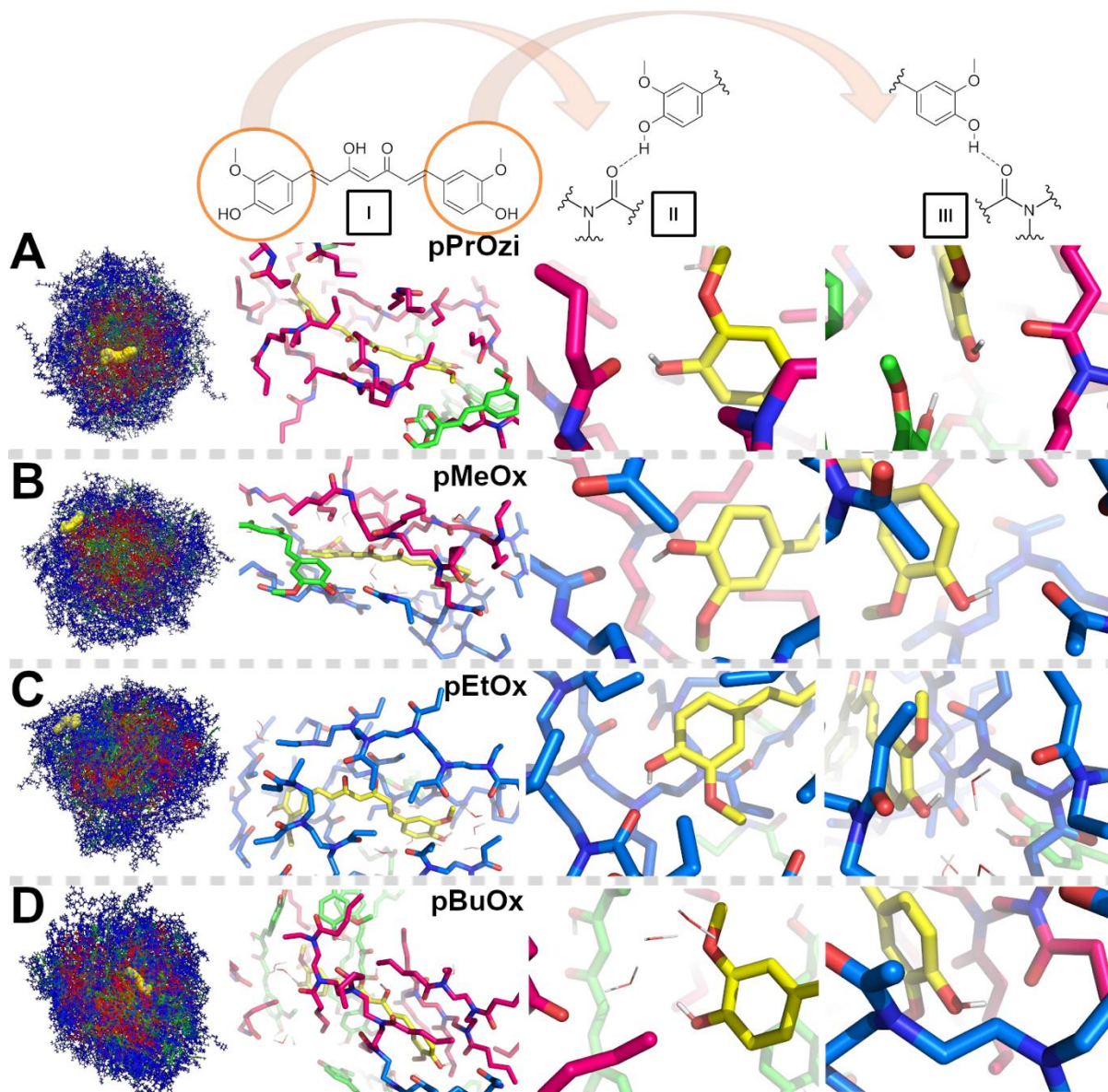
Figure 7: Exemplary polymer-drug interactions. Snapshots of different micelles are shown with transparent polymers and drugs and a single selected CUR molecule shown as yellow VDW spheres. For this molecule images on the right show interactions with the polymers and other CUR molecules, with additional pictures showing specifically both phenolic hydroxyl groups. Examples of CUR molecules near (A) pPrOzi, (B) pMeOx, (C) pEtOx and (D) pBuOx are illustrated, showing residues within 5 Å of the respective drug. Additional 2D polymer-drug interaction fingerprints for the examples shown are given in Figure S7 and S8.

Hydrogen bond analysis

As the described H-bonds might be crucial for explaining differences in drug loading capacities, these

were analyzed in more detail. The ratio between CUR-B and CUR-A H-bonds is highest for the case of

the A-pPrOzi-A systems (Figure 8), in line with higher drug loadings within the core (see above).
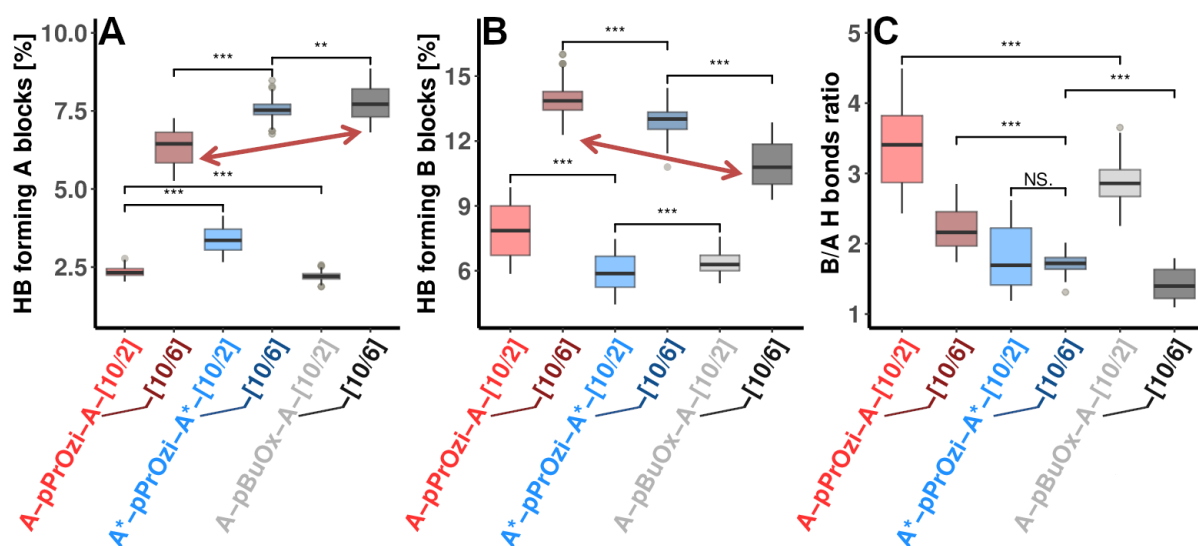
Figure 8: Percentage of (A) A block oxygens and (B) B block oxygens forming H-bonds with CUR molecules. (C) Ratio between percentage of H-bond forming B blocks and A blocks. Levels of significance for differences in median values are marked (p-values: *** = <0.001, ** = <0.01, * = <0.05, NS. = not significant).

RDF analyses provide further insight into the differences between the systems regarding these H-bonds (Figure 9). For the A blocks, A*-pPrOzi-A*-[10/2] and A*-pPrOzi-A*-[10/6] (along with A-pBuOx-A-[10/6]) show higher peaks than the other systems (first maximum at 2.8 Å, Figure 9A-I), corroborating the hypothesis of overall increased drug-polymer interactions within pEtOx-based shells compared to the pMeOx-based structures. Two additional smaller maxima can be found for the latter (4 – 8 Å, Figure 9A-II and 9A-IV), which can represent other oxygens of the same CUR molecule (e.g. the keto-enol group), but also other drug molecules in the vicinity. In contrast, pEtOx-based systems show only one additional broader peak (Figure 9A-III). For the B blocks, [10/6] systems show lower values than [10/2] systems as more drugs are located in the outer shell (Figure 9B). For each ratio though, A-pPrOzi-A systems show the highest peaks, reflecting the higher loading within the core. The first peak can also be found at 2.8 Å (Figure 9B-I), followed by several smaller local maxima between 4 and 8 Å (Figure 9B-II, 9B-III and 9B-V). Interestingly, these additional peaks are similar for pPrOzi-based structures whereas for pBuOx-based systems the most distant peak at around 7 Å (Figure 9B-IV) essentially vanishes. Findings from these RDF analyses clearly hint at distinctly different orderings of CUR molecules within micelles depending on the types of monomers interacting with the cargo.
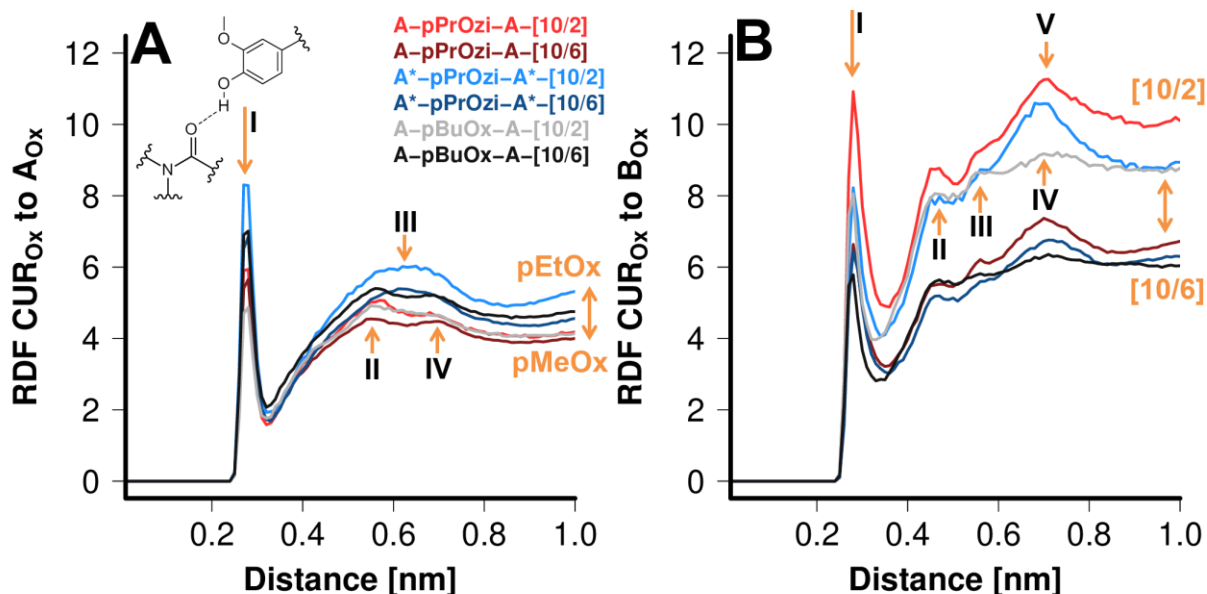
Figure 9: RDF plots describing the normalized radial atom density of (A) CUR oxygens around each A block polymer oxygen and (B) B block polymer oxygen. Detected peaks up to 1 nm distance are labeled, with the first resembling the polymer-drug H-bonding.

We further investigated the lifetime of such interactions, by calculating the respective autocorrelation functions applying distance cutoffs in accordance with the first minima in the RDF plots described above (3.3 Å for A blocks and 3.6 Å for B blocks). With the exception of A-pBuOx-A-[10/2].2 A blocks generally show longer lifetimes at lower loadings where fewer CUR molecules are located in the outer regions of the micelles (Figure 10A), albeit no difference between pMeOx and pEtOx is noted. Lifetimes between systems containing the same A or B blocks can be expected to differ, as changes in hydration, local drug concentration in core and shell areas and the size of the interfacial area between A and B blocks (where drugs are in contact with different types of repeat units) depend on the structure of the whole ABA-triblock copolymer but affect disruption of the investigated H-bonds. In conclusion though, the findings for the B blocks (Figure 10B) corroborate previous fluorescence upconversion studies, in which greater interaction lifetimes were also detected for pBuOx-based structures, which were interpreted as a result of lower CUR mobility.[17] Our MD experiments corroborate that micelles bearing pPrOzi hydrophobic domains with a much higher LC actually establish weaker interactions with the cargo than pBuOx.
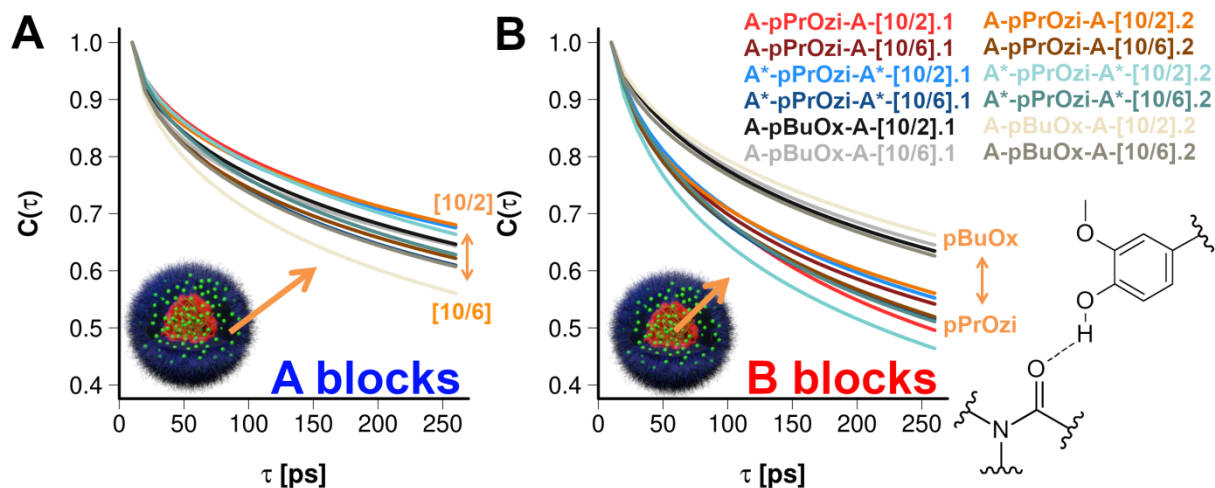
Figure 90: Exponential decay fits for hydrogen bond time autocorrelation functions $C(\tau)$ of H-bonds between phenolic CUR hydroxyl groups and (A) A blocks as well as (B) B blocks. Slower decays correspond to longer interaction lifetimes.

Distance analysis

We further investigated possible preferred orientations of polymer moieties around CUR molecules by calculating distance histograms, combining data from all systems based on the respective polymer types (Figure 11). Most histograms show very similar distributions, though some smaller differences are noticeable; as A-pPrOzi-A systems showed a generally higher drug loading within the core, PrOzi repeat units are more likely to be found near CUR molecules compared to B block monomers of systems containing A*-pPrOzi-A* or A-pBuOx-A (Figure 11A-I to 11A-III, 11B-I to 11B-III and 11C-I). This is also the case for the highest peak in Figure 11B-II, resembling H-bonds between the polymer oxygens and the phenolic hydroxyl groups. For the case of A-pBuOx-A, small additional peaks are detectable (Figure 11A-I and 11C-I). Additionally, the maxima are shifted around 1 Å closer in comparison to A-pPrOzi-A and A*-pPrOzi-A* (Figure 11A-III, 11C-II and 11C-III). This suggests that A-pBuOx-A (with overall lower loading in the core than A-pPrOzi-A) is able to approach CUR molecules more closely, especially the keto-enol group via its longer sidechain, which may result in a tighter packing of the cargo (possibly corroborating previous fluorescence uptime conversion studies,[17] see above). With respect to the A blocks, most histograms are comparable between the different systems, with the exception of the pEtOx sidechains that show larger distances to the aromatic drug moieties in comparison to pMeOx (Figure 11A-VI). Overall, these analyses illustrate only subtle differences between the orientations of the different monomer types around CUR molecules. Most distances show rather broad peaks, with the exception of the case involving CUR-polymer H-bonds (Figure 11B-II and 11B-V). In contrast to the latter, possible H-bonds between polymer oxygens and keto-enol groups are not detected, shown by broader peaks at larger distances (Figures 9C-II and 9C-V). Thus, while RDF

23

484   analyses hint at different CUR orderings depending on the types of monomers interacting with the

485   cargo (Figure 9), differences in these histograms are overall very subtle.

486   Additional occupancy density hotspots of polymer moieties were calculated for all CUR molecules of

487   selected systems to complement these measurements (Figure S9). In each case the most pronounced

488   hotspot for the polymer carbonyl oxygen is found near the phenolic hydroxyl groups of the drug.

489   Densities of backbones are highest below and underneath the aromatic rings, whereas edges of the

490   CUR molecules were more often observed to be flanked by polymer sidechains. Polymer amides near

491   aromatic drug moieties could promote further interactions, as was recently observed for the case of

492   poly(2-phenyl-2-oxazine)-based structures[79] in addition to aromatic amino acids.[29] In contrast to

493   hotspots around the aromatic rings, densities around the keto-enol tautomer are much more diffuse for

494   all polymer moieties, suggesting, once more, only weak interactions with this functional group.
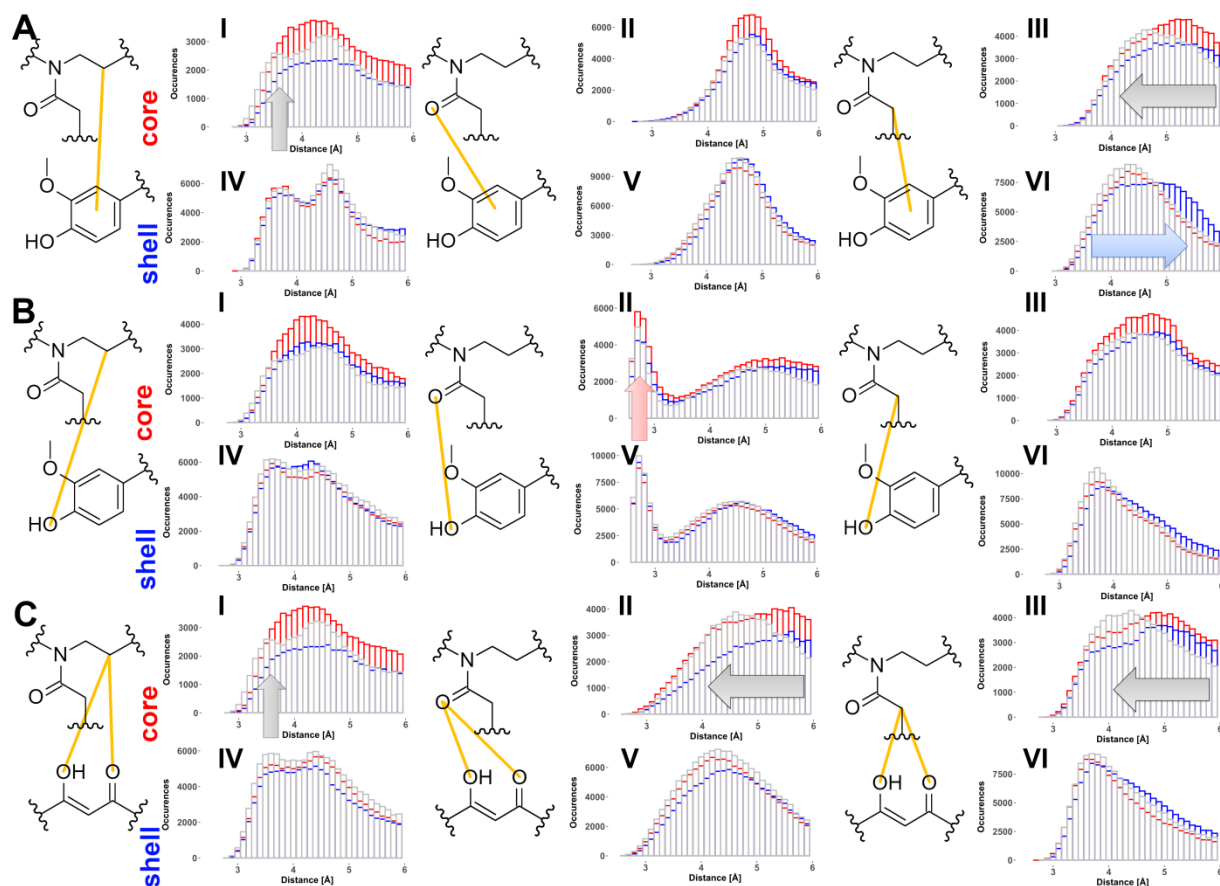
Figure 11: Histograms for distances between different polymer moieties (backbones, oxygens, sidechains) and CUR moieties (A = rings; B = hydroxyl groups; C = keto-enol oxygens), marked with yellow lines. In each case values for B blocks are shown on top (labels I to III) and values for A blocks on bottom (labels IV to VI). Data is shown in each plot combined for all A-pPrOzi-A (red), A*-pPrOzi-A* (blue) and A-pBuOx-A systems (gray).

501   *Model systems*

502   Finally, to collect more statistics on the characterized polymer-drug interactions, smaller model

503   systems were built via packmol (~ 5 nm box lengths) and simulated for at least 2 µs. These were

504   modeled with shorter homooligomers (hexamers), as well as drug and water atom densities in

505   accordance with core and shell areas derived from the first replicas of the full micelle after 1.75 µs of

506   simulation. Even though these correspond to conditions during the equilibration phase at elevated

507   temperatures, differences in hydrogen bond autocorrelation functions between repeat units, collected

508   for the whole trajectories, qualitatively agree with findings for larger systems (Figure 10). Overall, A

509   blocks showed longer lifetimes for the case of lower drug loadings (Figure S10A), whereas, within the

510   core, H-bonds formed via pBuOx B blocks showed slower decays compared to systems containing

511   pPrOzi (Figure S10B). Differences in absolute values can result from the usage of shorter, inherently

512   more flexible hexamers.

513   These smaller model systems were further used to perform a so-called g3 analysis in an analogous

514   way as recently performed for lipid bilayers.[65] Herein, intra-residue radial-angular three-particle

515   distributions of each monomer of all systems were analyzed to create heatmaps. Similarities of these

516   were summed into a single matrix which was subsequently reduced to 2D data via unsupervised

517   machine learning methods (t-SNE, DBScan, PCA). This procedure was performed in order to detect

518   additional potential differences in monomer conformations (Figure 12). In order to compare all

519   polymers analogously, we analyzed the distributions for four atoms found in every monomer type: the

520   amide nitrogen and oxygen, as well as the first sidechain carbon atom and the second backbone

521   carbon atom of the respective residue (Figure 12A, top right). Due to much shorter residues in

522   comparison to e.g. lipids and the limited selection of atoms, the resulting heatmaps showed only a few

523   hotspots (Figure 12B, as well as S11 and S12). 3 clusters were found by the dimensionality reduction

524   algorithm, whereas the biggest cluster 3 contains almost all pOx monomers (Figure 12C). In contrast,

525   pPrOzi monomers are nearly equally divided into clusters 1 and 2. While heatmaps of clusters 2 and 3

526   are very similar, cluster 1 contains mostly pPrOzi monomers with distinctly different conformations

527   according to the distances along PC1 in the PCA. Visual inspection of exemplary monomers reveals

528   that these are more likely to contain *trans* arrangements of the monomer alkyl sidechain with respect

529   to the backbone of the respective residue (Figure 12A). In contrast, pOx monomers make up only

530   about 20 % of this cluster (Figure 12D).
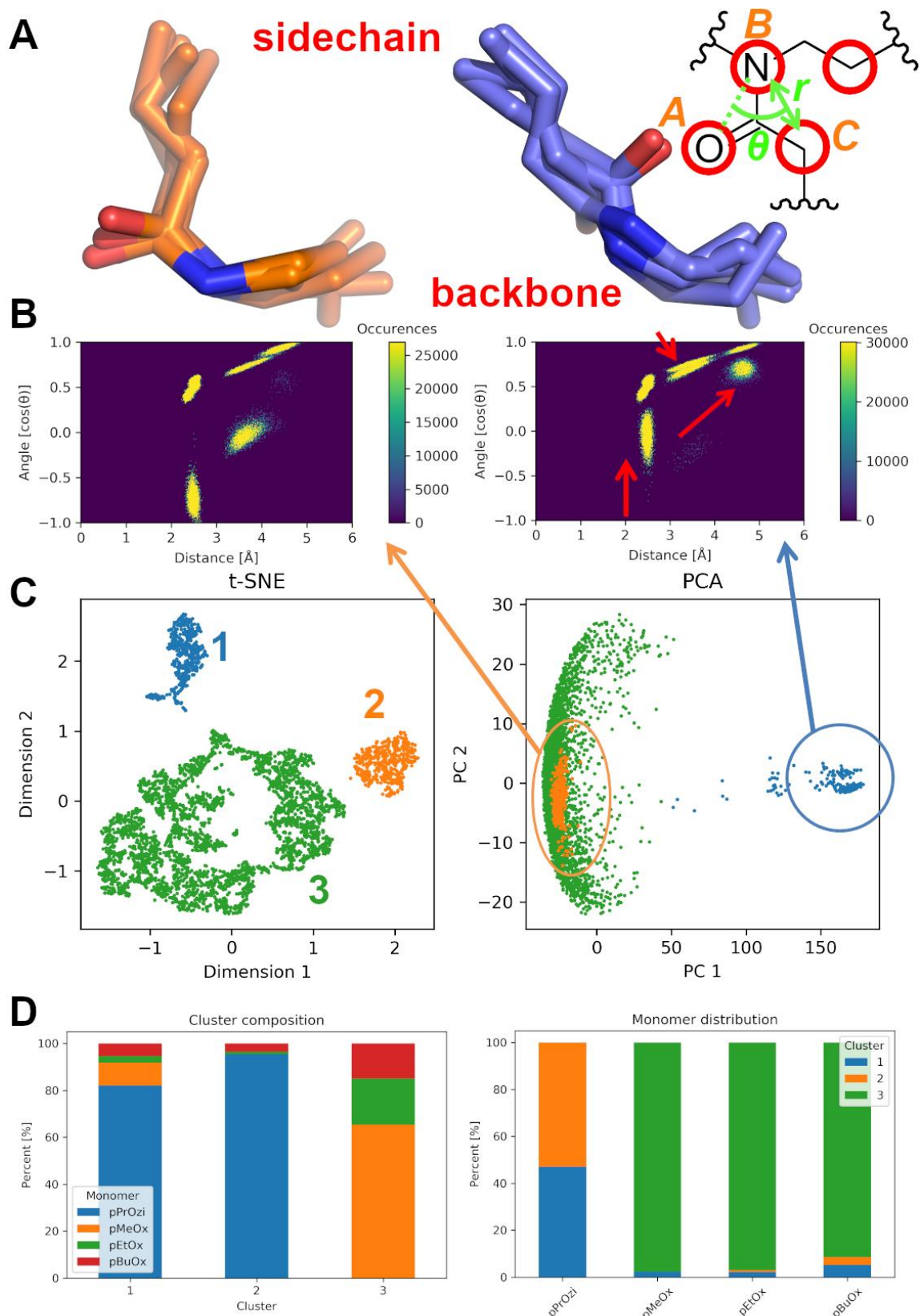
Figure 10: Results from g3 analysis. (A) Conformations of exemplary pPrOzi residues (showing every 10 ns of the last 50 ns) found in clusters 1 and 2, with atoms selected for analysis marked in the top right. (B) Corresponding g3 heatmaps of residues from (A), with red arrows indicating changes on the right. (C) Dimensionality reduction showing each monomer as a point in a 2D plot after t-SNE and subsequent PCA. (D) Cluster composition (left) and distribution of monomer types (right).

537 Based on these findings, dihedral angles in the larger micelle systems were further investigated

538 (Figure 13). Interestingly, pBuOx shows a strongly increased ratio between *cis* and *trans* oriented alkyl

539 sidechains (1:1) for repeat units found near CUR. In contrast, this ratio stays constant (mostly *trans*)

540 for the case of pPrOzi. Thus, g3 analysis combined with subsequent angle analyses on larger systems

541 suggests that the BuOx repeat units are affected by CUR loading with regard to their sidechain

542 orientations, whereas PrOzi repeat units, bearing an additional methylene group within the backbone

543 not directly bound to any tertiary amide, retain the same percentage of *trans* arrangements of alkyl

544 sidechains near the hydrophobic cargo. This could possibly be a deciding factor for the previously

545 experimentally determined overall preference of pOzi over pOx monomers for CUR loading.[10]

546
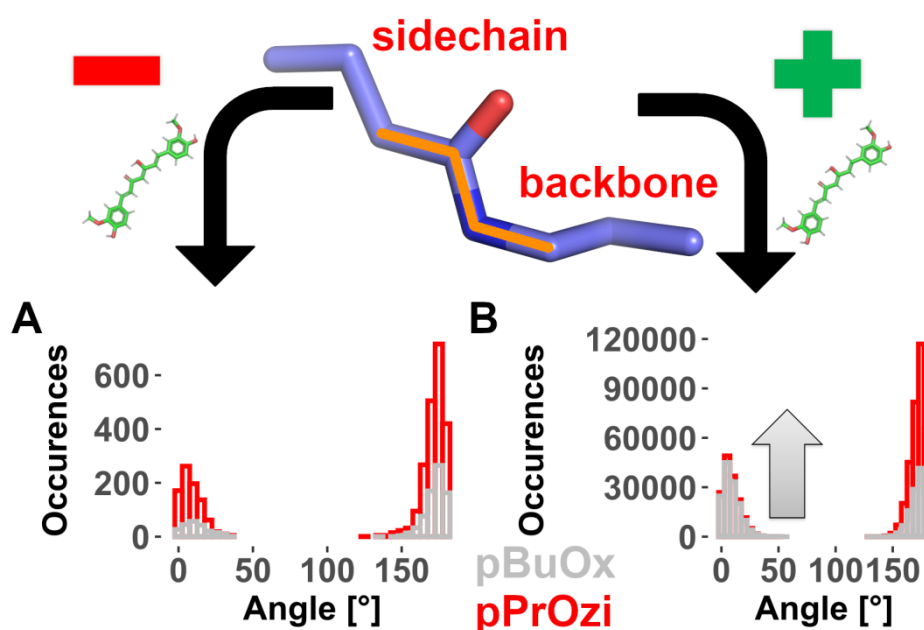
Figure 113: Distributions of dihedral angles measured between the first sidechain carbon atoms, the
carbonyl carbon atoms, the amide nitrogens and the first backbone carbon atoms (marked orange).
These are shown separately for monomers with a minimum distance of (A) > 8 Å (minus sign) and (B)
< 4 Å (plus sign) to any CUR molecule (pPrOzi = red, pBuOx = gray). Values are summed up for every
nanosecond in the last 100 ns.

552 Smaller model systems are often built as a stand-in for investigations of much larger polymeric

553 structures, including pseudo-micelles with shorter / fewer polymers and drugs.[38,80–82] To our

554 knowledge, this is the first time that additional sampling data on the individual hydrophobic and

555 hydrophilic micelle compartments based on specific conditions obtained from initial all-atom

556 simulations of larger structures with full-length polymers has been gathered. While we present here

557 only a very preliminary look into this, we believe this method could prove useful for other DDS

558 modeling studies as well, especially when applying resource-intensive machine learning approaches

559 such as the g3 analysis described above.

Conclusion

In this study, all-atom molecular dynamics simulations of nanoformulations of three exemplary ABA-triblock pOx/pOzi-based amphiphilic micelles at two different drug loadings were conducted on microsecond time scales, in order to dissect for the first time the underlying polymer-drug interactions and dynamics on a molecular level. For the case of A*-pPrOzi-A*, featuring EtOx hydrophilic repeat units, and especially A-pBuOx-A with lower experimental LC, the A blocks showed a greater extent of entanglement with B blocks, which might impact solubilization and colloidal stability of such a DDS. In agreement with previous experimental studies,[11,14] A-pPrOzi-A showed higher hydration of the shell in comparison to the case for A*-pPrOzi-A* with the more hydrophobic pEtOx corona; it also contained more drugs within the core than the other structures. At higher [10/6] loadings, more drugs could be found on the micelle surface, which corroborates earlier experimental findings and is expected to reduce hydrophilicity of the corona, ultimately leading to micelle aggregation, as observed experimentally for A*-pPrOzi-A* and A-pBuOx-A systems at this loading (exceeding maximum LC). Analysis of polymer-drug interactions showed CUR effectively (physically and intermolecularly) cross-link chains via H-bonds between its phenolic hydroxyl groups and polymer carbonyl oxygens, corroborating previous NMR experiments.[13] In line with differences in drug distributions across micelles, H-bonds between CUR and B blocks were most commonly found for the case of A-pPrOzi-A, though lifetimes of such interactions were higher for pBuOx. This agrees with previous fluorescence studies, hinting at stronger interactions of CUR with the latter and could result from different sidechain conformations of pPrOzi compared to pBuOx.[17]

Admittedly, we must acknowledge the fact that the investigated systems were loosely pre-assembled based on experimentally derived structural models from previous studies, suggesting spherical micelles with A blocks positioned in the outer and B blocks in the inner core.[13,14] The amount of polymers constituting a micelle was not known *a priori*, but this could certainly impact multiple aspects of the resulting structures, e.g. thickness of the corona. While longer time scales (via future coarse-graining approaches) might help characterizing overall micelle structures, this study focused on and provides significant data for detailed analysis of local polymer-drug interactions. Important to note, such interaction patterns, involving H-bonds, are only accessible via all-atom simulations. We will now investigate systems involving e.g. different A and B blocks or therapeutically valuable drugs, such as paclitaxel with a higher LC for A-pBuOx-A.[10] Cheminformatics-driven prediction models have already helped in *a priori* designing optimized pOx/pOzi-based formulations.[83] With additional simulations we

591   aim to complement such approaches providing detailed insight into the underlying dynamics of these

592   DDS in future studies.

References

(1) Bunker, A.; Róg, T. Mechanistic Understanding From Molecular Dynamics Simulation in Pharmaceutical Research 1: Drug Delivery. *Front. Mol. Biosci.* **2020**, *7*, 604770. https://doi.org/10.3389/fmolb.2020.604770.

(2) Park, H.; Otte, A.; Park, K. Evolution of Drug Delivery Systems: From 1950 to 2020 and Beyond. *Journal of Controlled Release* **2022**, *342*, 53–65. https://doi.org/10.1016/j.jconrel.2021.12.030.

(3) Lübtow, M. M.; Haider, M. S.; Kirsch, M.; Klisch, S.; Luxenhofer, R. Like Dissolves Like? A Comprehensive Evaluation of Partial Solubility Parameters to Predict Polymer–Drug Compatibility in Ultrahigh Drug-Loaded Polymer Micelles. *Biomacromolecules* **2019**, *20* (8), 3041–3056. https://doi.org/10.1021/acs.biomac.9b00618.

(4) Vinod, N.; Hwang, D.; Azam, S.; Van Swearingen, A.; Wayne, E.; Fussell, S.; Sokolsky, M.; Pecot, C.; Kabanov, A. Preparation and Characterization of Poly(2-Oxazoline) Micelles for the Solubilization and Delivery of Water Insoluble Drugs. *BIO-PROTOCOL* **2021**, *11* (6). https://doi.org/10.21769/BioProtoc.3959.

(5) Luxenhofer, R.; Schulz, A.; Roques, C.; Li, S.; Bronich, T. K.; Batrakova, E. V.; Jordan, R.; Kabanov, A. V. Doubly Amphiphilic Poly(2-Oxazoline)s as High-Capacity Delivery Systems for Hydrophobic Drugs. *Biomaterials* **2010**, *31* (18), 4972–4979. https://doi.org/10.1016/j.biomaterials.2010.02.057.

(6) Lorson, T.; Lübtow, M. M.; Wegener, E.; Haider, M. S.; Borova, S.; Nahm, D.; Jordan, R.; Sokolski-Papkov, M.; Kabanov, A. V.; Luxenhofer, R. Poly(2-Oxazoline)s Based Biomaterials: A Comprehensive and Critical Update. *Biomaterials* **2018**, *178*, 204–280. https://doi.org/10.1016/j.biomaterials.2018.05.022.

(7) Zahoranová, A.; Luxenhofer, R. Poly(2-oxazoline)- and Poly(2-oxazine)-Based Self-Assemblies, Polyplexes, and Drug Nanoformulations—An Update. *Adv. Healthcare Mater.* **2021**, *10* (6), 2001382. https://doi.org/10.1002/adhm.202001382.

(8) de la Rosa, V. R. Poly(2-Oxazoline)s as Materials for Biomedical Applications. *Journal of Materials Science: Materials in Medicine* **2014**, *25* (5), 1211–1225. https://doi.org/10.1007/s10856-013-5034-y.

(9) Lava, K.; Verbraeken, B.; Hoogenboom, R. Poly(2-Oxazoline)s and Click Chemistry: A Versatile Toolbox toward Multi-Functional Polymers. *European Polymer Journal* **2015**, *65*, 98–111. https://doi.org/10.1016/j.eurpolymj.2015.01.014.

(10) Lübtow, M. M.; Hahn, L.; Haider, M. S.; Luxenhofer, R. Drug Specificity, Synergy and Antagonism in Ultrahigh Capacity Poly(2-Oxazoline)/Poly(2-Oxazine) Based Formulations. *Journal of the American Chemical Society* **2017**, *139* (32), 10980–10983. https://doi.org/10.1021/jacs.7b05376.

(11) Haider, M. S.; Lübtow, M. M.; Endres, S.; Forster, S.; Flegler, V. J.; Böttcher, B.; Aseyev, V.; Pöppler, A.-C.; Luxenhofer, R. Think Beyond the Core: Impact of the Hydrophilic Corona on Drug Solubilization Using Polymer Micelles. *ACS Appl. Mater. Interfaces* **2020**, *12* (22), 24531–24543. https://doi.org/10.1021/acsami.9b22495.

(12) Haider, M. S.; Luxenhofer, R. *Development of Poly(2-Oxazoline)s and Poly(2-Oxazine)s Based Formulation Library and Estimation of Polymer/Drug Compatibility.*; preprint; Chemistry, 2022. https://doi.org/10.26434/chemrxiv-2022-s8xc3.

(13) Pöppler, A.-C.; Lübtow, M. M.; Schlauersbach, J.; Wiest, J.; Meinel, L.; Luxenhofer, R. Loading Dependent Structural Model of Polymeric Micelles Encapsulating Curcumin by Solid-State NMR Spectroscopy. *Angewandte Chemie International Edition* **2019**. https://doi.org/10.1002/anie.201908914.

(14) Sochor, B.; Düdükcü, Ö.; Lübtow, M. M.; Schummer, B.; Jaksch, S.; Luxenhofer, R. Probing the Complex Loading-Dependent Structural Changes in Ultrahigh Drug-Loaded Polymer Micelles by Small-Angle Neutron Scattering. *Langmuir* **2020**, *36* (13), 3494–3503. https://doi.org/10.1021/acs.langmuir.9b03460.

647 (15) Lim, C.; Ramsey, J. D.; Hwang, D.; Teixeira, S. C. M.; Poon, C.; Strauss, J. D.; Rosen, E. P.;
648   Sokolsky-Papkov, M.; Kabanov, A. V. Drug-Dependent Morphological Transitions in Spherical and
649   Worm-Like Polymeric Micelles Define Stability and Pharmacological Performance of Micellar
650   Drugs. *Small* **2022**, *18* (4), 2103552. https://doi.org/10.1002/smll.202103552.
651 (16) Tomeh, M.; Hadianamrei, R.; Zhao, X. A Review of Curcumin and Its Derivatives as Anticancer
652   Agents. *International Journal of Molecular Sciences* **2019**, *20* (5), 1033.
653   https://doi.org/10.3390/ijms20051033.
654 (17) Lübtow, M. M.; Marciniak, H.; Schmiedel, A.; Roos, M.; Lambert, C.; Luxenhofer, R. Ultra-High to
655   Ultra-Low Drug-Loaded Micelles: Probing Host–Guest Interactions by Fluorescence
656   Spectroscopy. *Chemistry – A European Journal* **2019**, *25* (54), 12601–12610.
657   https://doi.org/10.1002/chem.201902619.
658 (18) Hahn, L.; Lübtow, M. M.; Lorson, T.; Schmitt, F.; Appelt-Menzel, A.; Schobert, R.; Luxenhofer, R.
659   Investigating the Influence of Aromatic Moieties on the Formulation of Hydrophobic Natural
660   Products and Drugs in Poly(2-Oxazoline)-Based Amphiphiles. *Biomacromolecules* **2018**, *19* (7),
661   3119–3128. https://doi.org/10.1021/acs.biomac.8b00708.
662 (19) Styliari, I. D.; Taresco, V.; Theophilus, A.; Alexander, C.; Garnett, M.; Laughton, C.
663   Nanoformulation-by-Design: An Experimental and Molecular Dynamics Study for Polymer Coated
664   Drug Nanoparticles. *RSC Adv.* **2020**, *10* (33), 19521–19533.
665   https://doi.org/10.1039/D0RA00408A.
666 (20) Hanwell, M. D.; Curtis, D. E.; Lonie, D. C.; Vandermeersch, T.; Zurek, E.; Hutchison, G. R.
667   Avogadro: An Advanced Semantic Chemical Editor, Visualization, and Analysis Platform. *J*
668   *Cheminform* **2012**, *4* (1), 17. https://doi.org/10.1186/1758-2946-4-17.
669 (21) O'Boyle, N. M.; Banck, M.; James, C. A.; Morley, C.; Vandermeersch, T.; Hutchison, G. R. Open
670   Babel: An Open Chemical Toolbox. *Journal of Cheminformatics* **2011**, *3* (1).
671   https://doi.org/10.1186/1758-2946-3-33.
672 (22) Wang, J.; Wolf, R. M.; Caldwell, J. W.; Kollman, P. A.; Case, D. A. Development and Testing of a
673   General Amber Force Field. *J. Comput. Chem.* **2004**, *25* (9), 1157–1174.
674   https://doi.org/10.1002/jcc.20035.
675 (23) Vanquelef, E.; Simon, S.; Marquant, G.; Garcia, E.; Klimerak, G.; Delepine, J. C.; Cieplak, P.;
676   Dupradeau, F.-Y. R.E.D. Server: A Web Service for Deriving RESP and ESP Charges and
677   Building Force Field Libraries for New Molecules and Molecular Fragments. *Nucleic Acids*
678   *Research* **2011**, *39* (suppl_2), W511–W517. https://doi.org/10.1093/nar/gkr288.
679 (24) Wang, F.; Becker, J.-P.; Cieplak, P.; Dupradeau, F.-Y. *R.E.D. Python: Object Oriented*
680   *Programming for Amber Force Fields*; 2013.
681 (25) Dupradeau, F.-Y.; Pigache, A.; Zaffran, T.; Savineau, C.; Lelong, R.; Grivel, N.; Lelong, D.;
682   Rosanski, W.; Cieplak, P. The R.E.D. Tools: Advances in RESP and ESP Charge Derivation and
683   Force Field Library Building. *Physical Chemistry Chemical Physics* **2010**, *12* (28), 7821.
684   https://doi.org/10.1039/c0cp00111b.
685 (26) Bayly, C. I.; Cieplak, P.; Cornell, W.; Kollman, P. A. A Well-Behaved Electrostatic Potential Based
686   Method Using Charge Restraints for Deriving Atomic Charges: The RESP Model. *The Journal of*
687   *Physical Chemistry* **1993**, *97* (40), 10269–10280. https://doi.org/10.1021/j100142a004.
688 (27) Frisch, M. J.; Trucks, G. W.; Schlegel, H. B.; Scuseria, G. E.; Robb, M. A.; Cheeseman, J. R.;
689   Scalmani, G.; Barone, V.; Petersson, G. A.; Nakatsuji, H.; Li, X.; Caricato, M.; Marenich, A. V.;
690   Bloino, J.; Janesko, B. G.; Gomperts, R.; Mennucci, B.; Hratchian, H. P.; Ortiz, J. V.; Izmaylov, A.
691   F.; Sonnenberg, J. L.; Williams; Ding, F.; Lipparini, F.; Egidi, F.; Goings, J.; Peng, B.; Petrone, A.;
692   Henderson, T.; Ranasinghe, D.; Zakrzewski, V. G.; Gao, J.; Rega, N.; Zheng, G.; Liang, W.;
693   Hada, M.; Ehara, M.; Toyota, K.; Fukuda, R.; Hasegawa, J.; Ishida, M.; Nakajima, T.; Honda, Y.;
694   Kitao, O.; Nakai, H.; Vreven, T.; Throssell, K.; Montgomery Jr., J. A.; Peralta, J. E.; Ogliaro, F.;
695   Bearpark, M. J.; Heyd, J. J.; Brothers, E. N.; Kudin, K. N.; Staroverov, V. N.; Keith, T. A.;
696   Kobayashi, R.; Normand, J.; Raghavachari, K.; Rendell, A. P.; Burant, J. C.; Iyengar, S. S.;
697   Tomasi, J.; Cossi, M.; Millam, J. M.; Klene, M.; Adamo, C.; Cammi, R.; Ochterski, J. W.; Martin, R.
698   L.; Morokuma, K.; Farkas, O.; Foresman, J. B.; Fox, D. J. *Gaussian 16 C.01*; Wallingford, CT,
699   2016.
700 (28) Maier, J. A.; Martinez, C.; Kasavajhala, K.; Wickstrom, L.; Hauser, K. E.; Simmerling, C. Ff14SB:
701   Improving the Accuracy of Protein Side Chain and Backbone Parameters from Ff99SB. *J. Chem.*
702   *Theory Comput.* **2015**, *11* (8), 3696–3713. https://doi.org/10.1021/acs.jctc.5b00255.
703 (29) Hauptstein, N.; Pouyan, P.; Kehrein, J.; Dirauf, M.; Driessen, M. D.; Raschig, M.; Licha, K.;
704   Gottschaldt, M.; Schubert, U. S.; Haag, R.; Meinel, L.; Sotriffer, C.; Lühmann, T. Molecular
705   Insights into Site-Specific Interferon-A2a Bioconjugates Originated from PEG, LPG, and PEtOx.
706   *Biomacromolecules* **2021**, *22* (11), 4521–4534. https://doi.org/10.1021/acs.biomac.1c00775.
707 (30) Lübtow, M. M.; Nelke, L. C.; Seifert, J.; Kühnemundt, J.; Sahay, G.; Dandekar, G.; Nietzer, S. L.;
708   Luxenhofer, R. Drug Induced Micellization into Ultra-High Capacity and Stable Curcumin
709   Nanoformulations: Physico-Chemical Characterization and Evaluation in 2D and 3D in Vitro

710   Models. *Journal of Controlled Release* **2019**, *303*, 162–180.
711   https://doi.org/10.1016/j.jconrel.2019.04.014.
712 (31) Moussa, Z.; Chebl, M.; Patra, D. Fluorescence of Tautomeric Forms of Curcumin in Different PH
713   and Biosurfactant Rhamnolipids Systems: Application towards on-off Ratiometric Fluorescence
714   Temperature Sensing. *Journal of Photochemistry and Photobiology B: Biology* **2017**, *173*, 307–
715   317. https://doi.org/10.1016/j.jphotobiol.2017.06.011.
716 (32) Wang, J.; Wang, W.; Kollman, P. A.; Case, D. A. Automatic Atom Type and Bond Type Perception
717   in Molecular Mechanical Calculations. *Journal of Molecular Graphics and Modelling* **2006**, *25* (2),
718   247–260. https://doi.org/10.1016/j.jmgm.2005.12.005.
719 (33) Sousa da Silva, A. W.; Vranken, W. F. ACPYPE - AnteChamber PYthon Parser InterfacE. *BMC
720   Research Notes* **2012**, *5* (1). https://doi.org/10.1186/1756-0500-5-367.
721 (34) D.A. Case; H.M. Aktulga; K. Belfon; I.Y. Ben-Shalom; J.T. Berryman; S.R. Brozell; D.S. Cerutti;
722   T.E. Cheatham, III; G.A. Cisneros; V.W.D. Cruzeiro; T.A. Darden; R.E. Duke; G. Giambasu; M.K.
723   Gilson; H. Gohlke; A.W. Goetz; R. Harris; S. Izadi; S.A. Izmailov; K. Kasavajhala; M.C. Kaymak;
724   E. King; A. Kovalenko; T. Kurtzman; T.S. Lee; S. LeGrand; P. Li; C. Lin; J. Liu; T. Luchko; R. Luo;
725   M. Machado; V. Man; M. Manathunga; K.M. Merz; Y. Miao; O. Mikhailovskii; G. Monard; H.
726   Nguyen; K.A. O'Hearn; A. Onufriev; F. Pan; S. Pantano; R. Qi; A. Rahnamoun; D.R. Roe; A.
727   Roitberg; C. Sagui; S. Schott-Verdugo; A. Shajan; J. Shen; C.L. Simmerling; N.R. Skrynnikov; J.
728   Smith; J. Swails; R.C. Walker; J. Wang; H. Wei; R.M. Wolf; X. Wu; Y. Xiong; Y. Xue; D.M. York; S.
729   Zhao; P.A. Kollman. *Amber 2022*; University of California, San Francisco, 2022.
730 (35) Labute, P. The Generalized Born/Volume Integral Implicit Solvent Model: Estimation of the Free
731   Energy of Hydration Using London Dispersion Instead of Atomic Surface Area. *Journal of
732   Computational Chemistry* **2008**, *29* (10), 1693–1698. https://doi.org/10.1002/jcc.20933.
733 (36) Martínez, L.; Andrade, R.; Birgin, E. G.; Martínez, J. M. PACKMOL: A Package for Building Initial
734   Configurations for Molecular Dynamics Simulations. *J. Comput. Chem.* **2009**, *30* (13), 2157–2164.
735   https://doi.org/10.1002/jcc.21224.
736 (37) Martínez, J. M.; Martínez, L. Packing Optimization for Automated Generation of Complex
737   System's Initial Configurations for Molecular Dynamics and Docking. *Journal of Computational
738   Chemistry* **2003**, *24* (7), 819–825. https://doi.org/10.1002/jcc.10216.
739 (38) Razavilar, N.; Hanna, G. Molecular-Level Insights into the Diffusion of a Hydrophobic Drug in a
740   Disordered Block Copolymer Micelle by Molecular Dynamics Simulation. *Macromolecular Theory
741   and Simulations* **2022**, *31* (2), 2100060. https://doi.org/10.1002/mats.202100060.
742 (39) Dahanayake, R.; Dormidontova, E. E. Molecular Structure and Co-Solvent Distribution in PPO–
743   PEO and Pluronic Micelles. *Macromolecules* **2022**, acs.macromol.2c01206.
744   https://doi.org/10.1021/acs.macromol.2c01206.
745 (40) Jorgensen, W. L.; Chandrasekhar, J.; Madura, J. D.; Impey, R. W.; Klein, M. L. Comparison of
746   Simple Potential Functions for Simulating Liquid Water. *The Journal of Chemical Physics* **1983**, *79*
747   (2), 926–935. https://doi.org/10.1063/1.445869.
748 (41) Shirts, M. R.; Klein, C.; Swails, J. M.; Yin, J.; Gilson, M. K.; Mobley, D. L.; Case, D. A.; Zhong, E.
749   D. Lessons Learned from Comparing Molecular Dynamics Engines on the SAMPL5 Dataset.
750   *Journal of Computer-Aided Molecular Design* **2017**, *31* (1), 147–161.
751   https://doi.org/10.1007/s10822-016-9977-1.
752 (42) Abraham, M. J.; Murtola, T.; Schulz, R.; Pall, S.; Smith, J. C.; Hess, B.; Lindahl, E. GROMACS:
753   High Performance Molecular Simulations through Multi-Level Parallelism from Laptops to
754   Supercomputers. *SoftwareX* **2015**, *1–2*, 19–25.
755 (43) Bussi, G.; Donadio, D.; Parrinello, M. Canonical Sampling through Velocity Rescaling. *The
756   Journal of Chemical Physics* **2007**, *126* (1), 014101. https://doi.org/10.1063/1.2408420.
757 (44) Hockney, R. .; Goel, S. .; Eastwood, J. . Quiet High-Resolution Computer Models of a Plasma.
758   *Journal of Computational Physics* **1974**, *14* (2), 148–158. https://doi.org/10.1016/0021-
759   9991(74)90010-2.
760 (45) Darden, T.; York, D.; Pedersen, L. Particle Mesh Ewald: An $N \cdot \log(N)$ Method for Ewald Sums in
761   Large Systems. *The Journal of Chemical Physics* **1993**, *98* (12), 10089–10092.
762   https://doi.org/10.1063/1.464397.
763 (46) Hess, B.; Bekker, H.; Berendsen, H. J. C.; Fraaije, J. G. E. M. LINCS: A Linear Constraint Solver
764   for Molecular Simulations. *Journal of Computational Chemistry* **1997**, *18* (12), 1463–1472.
765   https://doi.org/10.1002/(SICI)1096-987X(199709)18:12<1463::AID-JCC4>3.0.CO;2-H.
766 (47) Parrinello, M.; Rahman, A. Crystal Structure and Pair Potentials: A Molecular-Dynamics Study.
767   *Phys. Rev. Lett.* **1980**, *45* (14), 1196–1199. https://doi.org/10.1103/PhysRevLett.45.1196.
768 (48) Parrinello, M.; Rahman, A. Polymorphic Transitions in Single Crystals: A New Molecular
769   Dynamics Method. *Journal of Applied Physics* **1981**, *52* (12), 7182–7190.
770   https://doi.org/10.1063/1.328693.
771 (49) Parrinello, M.; Rahman, A. Strain Fluctuations and Elastic Constants. *The Journal of Chemical
772   Physics* **1982**, *76* (5), 2662–2666. https://doi.org/10.1063/1.443248.

773   (50) Karabin, M.; Stuart, S. J. Simulated Annealing with Adaptive Cooling Rates. *J. Chem. Phys.* **2020**,
774   *153* (11), 114103. https://doi.org/10.1063/5.0018725.
775   (51) S. Kirkpatrick; C. D. Gelatt Jr.; M. P. Vecchi. Optimization by Simulated Annealing. *Science* **1983**,
776   *220* (4598), 671–680.
777   (52) Gowers, R.; Linke, M.; Barnoud, J.; Reddy, T.; Melo, M.; Seyler, S.; Domański, J.; Dotson, D.;
778   Buchoux, S.; Kenney, I.; Beckstein, O. MDAnalysis: A Python Package for the Rapid Analysis of
779   Molecular Dynamics Simulations; Austin, Texas, 2016; pp 98–105.
780   https://doi.org/10.25080/Majora-629e541a-00e.
781   (53) Michaud-Agrawal, N.; Denning, E. J.; Woolf, T. B.; Beckstein, O. MDAnalysis: A Toolkit for the
782   Analysis of Molecular Dynamics Simulations. *J. Comput. Chem.* **2011**, *32* (10), 2319–2327.
783   https://doi.org/10.1002/jcc.21787.
784   (54) Bauer, D. F. Constructing Confidence Sets Using Rank Statistics. *Journal of the American*
785   *Statistical Association* **1972**, *67* (339), 687–690.
786   https://doi.org/10.1080/01621459.1972.10481279.
787   (55) Hollander, M.; A. Wolfe, D.; Chicken, E. *Nonparametric Statistical Methods*, 1st ed.; Wiley Series
788   in Probability and Statistics; Wiley, 2015. https://doi.org/10.1002/9781119196037.
789   (56) Humphrey, W.; Dalke, A.; Schulten, K. VMD: Visual Molecular Dynamics. *J. Mol. Graphics* **1996**,
790   *14*, 33–36.
791   (57) *The PyMOL Molecular Graphics System, Version 2.0 Schrödinger, LLC.*
792   (58) Bouysset, C.; Fiorucci, S. ProLIF: A Library to Encode Molecular Interactions as Fingerprints. *J*
793   *Cheminform* **2021**, *13* (1), 72. https://doi.org/10.1186/s13321-021-00548-6.
794   (59) Landrum, G.; Tosco, P.; Kelley, B.; Ric; Sriniker; Gedeck; Vianello, R.; NadineSchneider;
795   Cosgrove, D.; Kawashima, E.; Dalke, A.; N, D.; Jones, G.; Cole, B.; Swain, M.; Turk, S.;
796   AlexanderSavelyev; Vaucher, A.; Wójcikowski, M.; Ichiru Take; Probst, D.; Ujihara, K.; Scalfani, V.
797   F.; Godin, G.; Pahl, A.; Francois Berenger; JLVarjo; Strets123; JP; DoliathGavid. *Rdkit/Rdkit:*
798   *2022_03_5 (Q1 2022) Release*; Zenodo, 2022. https://doi.org/10.5281/ZENODO.591637.
799   (60) Zhao; Ma; Li; De Nicola; Yu; Dong. Micellization of Pluronic P123 in Water/Ethanol/Turpentine Oil
800   Mixed Solvents: Hybrid Particle–Field Molecular Dynamic Simulation. *Polymers* **2019**, *11* (11),
801   1806. https://doi.org/10.3390/polym11111806.
802   (61) Todeschini, R.; Consonni, V. Descriptors from Molecular Geometry. In *Handbook of*
803   *Chemoinformatics*; Gasteiger, J., Ed.; Wiley-VCH Verlag GmbH: Weinheim, Germany, 2008; pp
804   1004–1033. https://doi.org/10.1002/9783527618279.ch37.
805   (62) Gowers, R. J.; Carbone, P. A Multiscale Approach to Model Hydrogen Bonding: The Case of
806   Polyamide. *The Journal of Chemical Physics* **2015**, *142* (22), 224907.
807   https://doi.org/10.1063/1.4922445.
808   (63) Sukhomlinov, S. V.; Müser, M. H. A Mixed Radial, Angular, Three-Body Distribution Function as a
809   Tool for Local Structure Characterization: Application to Single-Component Structures. *J. Chem.*
810   *Phys.* **2020**, *152* (19), 194502. https://doi.org/10.1063/5.0007964.
811   (64) Sukhomlinov, S. V.; Müser, M. H. Stress Anisotropy Severely Affects Zinc Phosphate Network
812   Formation. *Tribology Letters* **2021**, *69* (3). https://doi.org/10.1007/s11249-021-01462-6.
813   (65) Davies, M.; Reyes-Figueroa, A. D.; Gurtovenko, A. A.; Frankel, D.; Karttunen, M. *The Structure of*
814   *the Enigmatic Ripple Phase in Saturated Bilayers Resolved: Machine Learning Reveals Four Lipid*
815   *Populations*; preprint; Biophysics, 2021. https://doi.org/10.1101/2021.11.25.470048.
816   (66) Wang, Z.; Bovik, A. C.; Sheikh, H. R.; Simoncelli, E. P. Image Quality Assessment: From Error
817   Visibility to Structural Similarity. *IEEE Transactions on Image Processing* **2004**, *13* (4), 600–612.
818   https://doi.org/10.1109/TIP.2003.819861.
819   (67) Maaten, L. van der; Hinton, G. Visualizing Data Using T-SNE. *Journal of Machine Learning*
820   *Research* **2008**, *9* (86), 2579–2605.
821   (68) Schubert, E.; Sander, J.; Ester, M.; Kriegel, H. P.; Xu, X. DBSCAN Revisited, Revisited: Why and
822   How You Should (Still) Use DBSCAN. *ACM Trans. Database Syst.* **2017**, *42* (3), 1–21.
823   https://doi.org/10.1145/3068335.
824   (69) Buslaev, P.; Gordeliy, V.; Grudinin, S.; Gushchin, I. Principal Component Analysis of Lipid
825   Molecule Conformational Changes in Molecular Dynamics Simulations. *Journal of Chemical*
826   *Theory and Computation* **2016**, *12* (3), 1019–1028. https://doi.org/10.1021/acs.jctc.5b01106.
827   (70) Tsai, E.; Gallage Dona, H. K.; Tong, X.; Du, P.; Novak, B.; David, R.; Rick, S. W.; Zhang, D.;
828   Kumar, R. Unraveling the Role of Charge Patterning in the Micellar Structure of Sequence-
829   Defined Amphiphilic Peptoid Oligomers by Molecular Dynamics Simulations. *Macromolecules*
830   **2022**, *55* (12), 5197–5212. https://doi.org/10.1021/acs.macromol.2c00141.
831   (71) Lee, S. M.; Bond, N.; Callaway, C.; Clark, B.; Farmer, E.; Mallard, M.; Jang, S. S. Dissipative
832   Particle Dynamics Simulation of Multicompartment Micelle Nanoreactor with Channel for
833   Reactants. *RSC Advances* **2018**, *8* (66), 37866–37871. https://doi.org/10.1039/C8RA07023G.
834   (72) Hoogenboom, R.; Schlaad, H. Thermoresponsive Poly(2-Oxazoline)s, Polypeptoids, and
835   Polypeptides. *Polym. Chem.* **2017**, *8* (1), 24–40. https://doi.org/10.1039/C6PY01320A.

836   (73) Bloksma, M. M.; Paulus, R. M.; van Kuringen, H. P. C.; van der Woerdt, F.; Lambermont-Thijs, H.
837   M. L.; Schubert, U. S.; Hoogenboom, R. Thermoresponsive Poly(2-Oxazine)S. *Macromol. Rapid*
838   *Commun.* **2012**, *33* (1), 92–96. https://doi.org/10.1002/marc.201100587.
839   (74) Dalgakiran, E.; Tatlipinar, H. The Role of Hydrophobic Hydration in the LCST Behaviour of
840   POEGMA ₃₀₀ by All-Atom Molecular Dynamics Simulations. *Physical Chemistry Chemical Physics*
841   **2018**, *20* (22), 15389–15399. https://doi.org/10.1039/C8CP02026D.
842   (75) Yang, C.; Lu, D.; Liu, Z. How PEGylation Enhances the Stability and Potency of Insulin: A
843   Molecular Dynamics Simulation. *Biochemistry* **2011**, *50* (13), 2585–2593.
844   https://doi.org/10.1021/bi101926u.
845   (76) Luft, C. M.; Munusamy, E.; Pemberton, J. E.; Schwartz, S. D. A Classical Molecular Dynamics
846   Simulation Study of Interfacial and Bulk Solution Aggregation Properties of Dirhamnolipids. *The*
847   *Journal of Physical Chemistry B* **2020**, *124* (5), 814–827.
848   https://doi.org/10.1021/acs.jpcb.9b08800.
849   (77) Sohrabi, S.; Khedri, M.; Maleki, R.; Moraveji, M. K.; Ghasemy, E. In-Silico Tuning of Curcumin
850   Loading on PEG Grafted Chitosan: An Atomistic Simulation. *ChemistrySelect* **2021**, *6* (18), 4544–
851   4555. https://doi.org/10.1002/slct.202100354.
852   (78) Yadav, P.; Bandyopadhyay, A.; Chakraborty, A.; Sarkar, K. Enhancement of Anticancer Activity
853   and Drug Delivery of Chitosan-Curcumin Nanoparticle via Molecular Docking and Simulation
854   Analysis. *Carbohydrate Polymers* **2018**, *182*, 188–198.
855   https://doi.org/10.1016/j.carbpol.2017.10.102.
856   (79) Hahn, L.; Zorn, T.; Kehrein, J.; Kielholz, T.; Ziegler, A.-L.; Forster, S.; Sochor, B.; Lisitsyna, E. S.;
857   Durandin, N.; Laaksonen, T.; Aseyev, V.; Sotriffer, C.; Windbergs, M.; Pöppler, A.-C.; Luxenhofer,
858   R. *Unravelling a Novel Mechanism in Polymer Self-Assemblies: An Order-Order Transition Based*
859   *on Molecular Interactions between Hydrophilic and Hydrophobic Polymer Blocks*; preprint;
860   Chemistry, 2021. https://doi.org/10.26434/chemrxiv-2021-mjd8n-v2.
861   (80) Jha, P. K.; Larson, R. G. Assessing the Efficiency of Polymeric Excipients by Atomistic Molecular
862   Dynamics Simulations. *Mol. Pharmaceutics* **2014**, *11* (5), 1676–1686.
863   https://doi.org/10.1021/mp500068w.
864   (81) Razavilar, N.; Choi, P. Diffusivity of Cucurbitacin B in Water Swollen Polyethylene Oxide-b-
865   Polycaprolactone Matrices with Different PCL/PEO Weight Ratios. *Computational Materials*
866   *Science* **2016**, *118*, 97–102. https://doi.org/10.1016/j.commatsci.2016.03.014.
867   (82) Razavilar, N.; Choi, P. Molecular Dynamics Study of the Diffusivity of a Hydrophobic Drug
868   Cucurbitacin B in Pseudo-Poly(Ethylene Oxide- *b* -Caprolactone) Micelle Environments. *Langmuir*
869   **2014**, *30* (26), 7798–7803. https://doi.org/10.1021/la500572p.
870   (83) Alves, V. M.; Hwang, D.; Muratov, E.; Sokolsky-Papkov, M.; Varlamova, E.; Vinod, N.; Lim, C.;
871   Andrade, C. H.; Tropsha, A.; Kabanov, A. Cheminformatics-Driven Discovery of Polymeric Micelle
872   Formulations for Poorly Soluble Drugs. *Sci. Adv.* **2019**, *5* (6), eaav9784.
873   https://doi.org/10.1126/sciadv.aav9784.
874